

# Resolving the CO Snow Line in the Disk around HD 163296

Chunhua Qi<sup>1</sup>, Paola D'Alessio<sup>2</sup>, Karin I. Öberg<sup>1,3</sup>, David J. Wilner<sup>1</sup>, A. Meredith Hughes<sup>1,4,5</sup>, Sean M. Andrews<sup>1</sup>, Sandra Ayala<sup>2</sup>

## ABSTRACT

We report Submillimeter Array (SMA) observations of CO (J=2–1, 3–2 and 6–5) and its isotopologues (<sup>13</sup>CO J=2–1, C<sup>18</sup>O J=2–1 and C<sup>17</sup>O J=3–2) in the disk around the Herbig Ae star HD 163296 at  $\sim 2''$  (250 AU) resolution, and interpret these data in the framework of a model that constrains the radial and vertical location of the line emission regions. First, we develop a physically self-consistent accretion disk model with an exponentially tapered edge that matches the spectral energy distribution and spatially resolved millimeter dust continuum emission. Then, we refine the vertical structure of the model using wide range of excitation conditions sampled by the CO lines, in particular the rarely observed J=6–5 transition. By fitting <sup>13</sup>CO data in this structure, we further constrain the vertical distribution of CO to lie between a lower boundary below which CO freezes out onto dust grains ( $T \lesssim 19$  K) and an upper boundary above which CO can be photodissociated (the hydrogen column density from the disk surface is  $\lesssim 10^{21}$  cm<sup>-2</sup>). The freeze-out at 19 K leads to a significant drop in the gas-phase CO column density beyond a radius of  $\sim 155$  AU, a “CO snow line” that we directly resolve. By fitting the abundances of all CO isotopologues, we derive isotopic ratios of <sup>12</sup>C/<sup>13</sup>C, <sup>16</sup>O/<sup>18</sup>O and <sup>18</sup>O/<sup>17</sup>O that are consistent with quiescent interstellar gas-phase values. This detailed model of the HD 163296 disk demonstrates the potential of a staged, parametric technique for constructing unified gas and dust structure models and constraining the distribution of molecular abundances using resolved multi-transition, multi-isotope observations.

---

<sup>1</sup>Harvard–Smithsonian Center for Astrophysics, 60 Garden Street, MS 42, Cambridge, MA 02138, USA; cqi, koberg, dwilner, mhughes, sandrews@cfa.harvard.edu.

<sup>2</sup>Centro de Radioastronomía y Astrofísica, Universidad Nacional Autónoma de México, 58089 Morelia, Michoacán, México; p.dalessio@crya.unam.mx, sayala2001@gmail.com

<sup>3</sup>Hubble Fellow

<sup>4</sup>Department of Astronomy, University of California at Berkeley, 601 Campbell Hall, Berkeley, CA 94720, USA

<sup>5</sup>Miller Fellow

*Subject headings:* circumstellar matter —techniques: interferometric —planetary systems: protoplanetary disks —stars: individual(HD 163296) —ISM: abundances —radio lines: stars

## 1. Introduction

The disks around pre-main sequence stars are the reservoirs of raw material that represent the initial conditions for the formation of planetary systems. The spatial distribution of mass in these disks is a fundamental property, as it sets a constraint on the contents and orbital architectures of planetary systems. In that sense, measurements of disk densities and temperatures can provide strong, albeit complex, constraints on planet-forming scenarios. Because the dominant constituent of these disks is believed to be cold  $\text{H}_2$  gas that is generally unobservable, our knowledge of many disk properties (including mass) relies on the observation and interpretation of minor constituents. Dust has naturally been the focus of the most work on disk structure and evolution, as it dominates the opacity and emits bright continuum radiation (e.g., Andrews et al. 2009, 2010). However, converting those continuum surface brightnesses to disk (gas) densities is challenging due to the large uncertainties in the assumed dust properties (composition, size distribution, etc.) and the dust abundance relative to the gas, which may deviate substantially from the canonical interstellar value (0.01) and vary spatially in the disk. In principle, spectral line emission from trace gas species can provide complementary constraints on the disk structure, but the interpretation of the observations can also be difficult. These emission lines depend on the gas abundances that are set by chemical and physical processes, as well as the excitation conditions set by the local densities, temperatures, and incident radiation fields. With a dataset of sufficient quality, these complexities can be leveraged into powerful probes of otherwise inaccessible disk characteristics (e.g., Kamp et al. 2010).

The chemical property of CO, the most abundant molecule after  $\text{H}_2$ , is thought to be well understood in disks. The spatial distribution of gas-phase CO is expected to be shaped by photodissociation both near the star and high in the disk atmosphere, as well as by a depletion process when it freezes onto dust grains at low temperatures (below  $\sim 20$  K) at large radii and deep in the disk interior (e.g., Aikawa et al. 1996; Aikawa & Nomura 2006; Gorti & Hollenbach 2008). The peak abundance of CO is also predicted to be almost independent of radius, around  $10^{-4}$ , the typical value in molecular clouds (Aikawa & Nomura 2006). However, observational studies of CO emission from disks have yielded puzzling results. In general, the CO in disks is found to be under-abundant by factors of 10–100 compared to molecular clouds, a deficit usually attributed to CO depletion in cold, dense gas

(Dutrey et al. 1994, 1996, 1997; van Zadelhoff et al. 2001; Thi et al. 2004). However, multi-transition and multi-isotope CO studies report a wide range of relative depletions of CO and its isotopologues. For example, Dartois et al. (2003) finds that all of the CO isotopologues are depleted by an identical uniform factor of  $\sim 10$ , but Piétu et al. (2007) finds in a small sample of disks that the  $^{12}\text{CO}/^{13}\text{CO}$  ratios in the outer part of disks are much lower than the standard  $^{12}\text{C}/^{13}\text{C}$  ratio in the solar neighborhood: these low values were attributed to significant carbon fractionation. At the same time, both of these studies suggested that the outer radius derived from  $^{13}\text{CO}$  is smaller than the one derived from  $^{12}\text{CO}$  indicating their  $^{12}\text{CO}/^{13}\text{CO}$  ratios are abnormally large at the outer disk edge of their models, which leads to speculations on the importance of selective photo-dissociation due to self-shielding in the photolysis of gaseous CO (Dutrey et al. 2007). They also find that a large amount of CO remains gaseous at temperatures as low as 10 K. Possible explanations for the presence of the inferred cold CO include vertical mixing (Aikawa 2007) and photodesorption off dust grains (Hersant et al. 2009). All above depict a very complex picture of the distribution of CO gas in the disks, which remains to be explained by detailed chemical models combined with realistic physical disk structures. However, it is unclear, how much of these variations depend on the individual sources, and how much, if any, depends on the modeling approach.

A robust methodology for interpreting CO observations is a high priority for our efforts to constrain the total gas distribution in disks, and to provide a basis for interpreting observations of more complex molecules. In this study, we develop a modeling framework that is able to account for observations of both the dust continuum and CO line emission from a protoplanetary disk. Specifically, we combine a previously-established dust emission modeling formalism with multiple transitions, spatially resolved CO line data (CO J=2–1, 3–2 and 6–5,  $^{13}\text{CO}$  J=2–1,  $\text{C}^{18}\text{O}$  J=2–1 and  $\text{C}^{17}\text{O}$  J=3–2) to construct a simplified and internally self-consistent model of the disk around the Herbig Ae star HD 163296. At a distance of  $\sim 122$  pc (Perryman et al. 1997), this  $2.3 M_{\odot}$  star (spectral type A1; age  $\sim 4$  Myr) harbors a large disk with strong millimeter continuum and molecular line emission (Qi 2001; Thi et al. 2004; Natta et al. 2004). It does not seem to be associated with any known star-formation region, dark clouds, or reflection nebulae. The disk around HD 163296 exhibits a scattered light pattern extending out to a radius of  $\sim 500$  AU (Grady et al. 2000), perpendicular to a bipolar microjet traced by a chain of HH knots visible in coronagraphic observations (Devine et al. 2000; Grady et al. 2000; Wassell et al. 2006). Millimeter and submillimeter interferometric observations have explored this large disk and its Keplerian velocity field in low-J CO lines (Mannings & Sargent 1997; Isella et al. 2007). The large disk size and strong molecular emission make this system an excellent target for resolved millimeter observations and detailed modeling.

This paper is organized as follows. We describe the CO and mm continuum data in §2,

and present the main observational results in §3. Our extensive modeling effort is detailed in §4. We discuss the modeling results and compare with previous work on this subject in §5, and provide a brief summary in §6.

## 2. Observations

Observations of HD 163296 (RA:  $17^{\text{h}}56^{\text{m}}21^{\text{s}}.279$ , DEC:  $-21^{\circ}57'22''.09$ ; J2000.0) were conducted between 2005 August and 2010 September using the 8-antenna SMA<sup>1</sup> interferometer located atop Mauna Kea, Hawaii. Table 1 provides a general summary of the observational parameters.

For the observations of the CO 6–5 line, we used the correlator settings adopted by Qi et al. (2006) in their similar study of the TW Hya disk. At 690 GHz, there is no nearby quasar bright enough to use for phase referencing with the SMA. However, Callisto was located only  $10^{\circ}$  away from HD 163296 during our observation on 2007 March 20, and was monitored every 20 minutes for use in the gain and absolute flux calibration. At that time, Callisto had a diameter of  $1''.3$  and a zero-spacing flux density of 48.1 Jy at 690 GHz. Based on the uncertainties of the Callisto emission model, we estimate a 10% systematic uncertainty in this adopted flux scale. The 690 GHz continuum emission from HD 163296 was sufficiently bright (with a flux density of 7.5 Jy) that we could correct the gain response of the SMA with a single phase-only self-calibration iteration.

The observations of the CO 2–1 line took place on 2010 May 17 in the compact configuration and 2010 September 14 in the extended configuration. The correlator was configured to include 2048 channels in the 104 MHz segment of the correlator centered on the rest frequency of the line. The remaining 1.3 GHz of the correlator bandwidth in both sidebands were configured with a uniform spectral resolution of 256 channels in each 104 MHz correlator segment to achieve maximum continuum sensitivity. The weather was good on both nights, with the 225 GHz opacity just below 0.1 and stable atmospheric phase. The nearby quasar 1733-130 (10.5 degrees from the source) was used to calibrate the atmospheric and instrumental phase, and the solution was checked using the quasar 1911-201, which was included for a short period during each loop between source and calibrator. Uranus and Neptune were used as flux calibrators on September 14, yielding a 1733-130 flux of 2.71 Jy; Callisto was used to calibrate the May 17 flux, yielding a 1733-130 flux of 2.04 Jy.

---

<sup>1</sup>The Submillimeter Array is a joint project between the Smithsonian Astrophysical Observatory and the Academia Sinica Institute of Astronomy and Astrophysics, and is funded by the Smithsonian Institution and the Academia Sinica.

The observations of  $^{13}\text{CO}$  2–1 and  $\text{C}^{18}\text{O}$  2–1 were carried out simultaneously on 2010 May 15 in the compact configuration and 2010 September 11 in the extended configuration. The correlator configuration was identical to the CO 2–1 setup, except that the high resolution correlator chunk was centered on the rest frequency of  $^{13}\text{CO}$  2–1 with  $\text{C}^{18}\text{O}$  2–1 in a nearby low-resolution chunk. The remaining 1.2 GHz were devoted to uniform spectral resolution continuum observations. The weather was excellent on both nights with stable phase and 225 GHz opacity varying between 0.04 (primarily during the extended track) and 0.06. The same calibrators as for the CO(2-1) observations were used; the derived flux of 1733-130 was 2.35 on September 11 and 2.04 Jy on May 15.

The observation of the  $\text{C}^{17}\text{O}$  3–2 line took place on 2005 August 23 in the compact configuration. The correlator was configured with a uniform spectral resolution of 128 channels over 104 MHz, which provided 0.8 MHz frequency resolution. The nearby quasars 1833-210 and 1921-293 were used as the calibrators. Uranus was used as flux calibrator and the derived fluxes of 1833-210 and 1921-293 were 0.57 and 3.76 Jy, respectively.

The observations of the CO 3–2 observations were summarized in Hughes et al. (2011). All of the calibration was performed using the MIR software package<sup>2</sup>. Images of the continuum and the spectral lines were generated and CLEANed using standard techniques in the MIRIAD software package.

### 3. Results

Figure 1 shows the disk-averaged spectra of the CO J=2–1, 3–2 and 6–5 lines, along with the J=2–1 lines of  $^{13}\text{CO}$  and  $\text{C}^{18}\text{O}$  and the J=3–2 line of  $\text{C}^{17}\text{O}$  3–2. These spectra were extracted from the SMA channel maps in  $10''$  square boxes centered on HD 163296, except for the CO 6–5 line. That fainter spectrum was produced from a  $4''$ -wide box chosen to cover the area with statistically significant emission. Each emission line shows the double-peaked velocity profile characteristic of disk rotation. The low-J CO lines have an additional feature in their spectra at  $V_{\text{LSR}} = 13 \text{ km s}^{-1}$ , which is distinctly offset from the disk kinematically and much more obvious in previous single-dish spectra (Thi et al. 2001, 2004). That feature is apparently spatially extended, and likely is associated with foreground and/or background molecular clouds. Table 2 lists the integrated intensities of the observed lines and the continuum flux densities. Note that the signal-to-noise ratios range from over 200 for the CO 2–1 line to  $\sim 10$  for the CO 6–5 and  $\text{C}^{17}\text{O}$  3–2 lines. Figure 2, 3 and 4 show the channel maps of all the transitions except for CO 3–2 which were presented in Hughes et al. (2011).

---

<sup>2</sup><http://www.cfa.harvard.edu/~cqi/mircook.html>

## 4. Analysis

As a first step in developing a framework for understanding the chemical structures of protoplanetary disks, we aim to interpret this suite of observations in the context of an internally self-consistent model for the physical conditions of the gas and dust in the HD 163296 disk. Our modeling analysis consists of three distinct stages. First, we construct a template two-dimensional model for the disk structure based on observations of the dust, using the broadband spectral energy distribution (SED) and the resolved millimeter continuum emission as diagnostics (§4.1). Second, we refine the vertical temperature distribution of that template structure based on the spatially resolved line ratios of the optically thick CO transitions (§4.2). And third, we constrain the radial and vertical CO abundance pattern using the emission from the more optically thin CO isotopologue transitions (§4.3).

### 4.1. Stage 1: Template Disk Structure Model

Our starting point is with a set of disk structures calculated following the prescription for a steady viscous accretion disk model (see D’Alessio et al. 1998, 1999, 2001, 2006). In these models, the gas surface density is determined based on the conservation of angular momentum flux and depends on the mass flow rate ( $\dot{M}$ ), viscosity coefficient  $\alpha$  (Shakura & Sunyaev 1973), and midplane temperature ( $T_0$ ), such that  $\Sigma \propto \dot{M}/\alpha T_0$ . We assume that  $\dot{M}$  is constant throughout the disk, but make an important structural modification from previous generations of these models. Motivated by the similarity solution for the time evolution of accretion disks (Hartmann et al. 1998) and recent millimeter-wave observations (Hughes et al. 2008), we allow the viscosity coefficient to vary radially such that  $\alpha = \alpha_0 \exp R/R_c$ . This change makes no difference at small radii ( $R \ll R_c$ ), but effectively adds an exponential taper to the surface density profile outside the characteristic radius,  $R_c$ . Although this modification mimics the  $\Sigma$  profile derived from the similarity solution models, it does not reproduce the predicted behavior of the mass flow rate as a function of radius. However, that  $\dot{M}$  profile is not expected to have any observable effects on the disk structure at these large radii, since stellar irradiation is a much more important heating mechanism than viscous dissipation in those regions.

For a given flow rate ( $\dot{M}$ ), viscosity coefficient ( $\alpha_0$ ), and characteristic radius ( $R_c$ ), the density and temperature structure of this model is determined as described by D’Alessio et al. (1998, 1999). We consider heating from the mechanical work of viscous dissipation (relevant only in the midplane of the inner disk), accretion shocks at the stellar surface, and passive stellar irradiation, and follow the radiative transfer of that energy with 1+1D calculations using the Eddington approximation and a set of mean dust opacities (gas opacities are con-

sidered negligible). The dust is assumed to be a mixture of segregated spheres composed of “astronomical” silicates and graphite, with abundances (relative to the total gas mass) of  $\zeta_{\text{sil}} = 0.004$  and  $\zeta_{\text{gra}} = 0.0025$  (Draine & Lee 1984): the “reference” dust-to-gas mass ratio is  $\zeta_{\text{ref}} = 0.0065$ . At any given location in the disk, the grain size ( $a$ ) distribution of these dust particles is assumed to be a power-law,  $n(a) \propto a^{-3.5}$ , between  $a_{\text{min}} = 0.005 \mu\text{m}$  and a specified  $a_{\text{max}}$ . We assume the disk has two grain populations, each with a different maximum size. The “small” grains are distributed in the disk atmosphere and have  $a_{\text{max}} = 0.25 \mu\text{m}$  (as in the interstellar medium), and the “big” grains are concentrated toward the midplane and have  $a_{\text{max}} = 1 \text{ mm}$ . Utilizing the dust settling prescription of D’Alessio et al. (2006), the “small” grain population in the upper disk layers is assumed to have a dust-to-gas mass ratio  $\epsilon\zeta_{\text{ref}}$  and the “big” grain population near the midplane has a dust-to-gas ratio determined so that mass is conserved at each radius. A smooth vertical transition between the two grain populations is made at a height  $z_{\text{big}}$  above the midplane.

The inner boundary of the structure model is taken to be the radius where silicates are sublimated (where  $T \approx 1500 \text{ K}$ ). Because this inner rim is irradiated by the photosphere of the central star (Natta et al. 2000; Dullemond et al. 2001) and the accretion shock at the stellar surface (Muzerolle et al. 2004) at a normal incidence angle, the material is heated to high temperatures and therefore extends (or “puffs” up) to a larger vertical height,  $z_{\text{wall}}$ . The radial structure of that “wall” feature (and its emergent spectrum) is calculated as described by D’Alessio et al. (2005). The structure model is truncated at 540 AU, large enough to have no effect on our analysis.

In the model calculations, we adopt the HD 163296 stellar parameters advocated by van den Ancker et al. (1998) –  $M_* = 2.3 M_{\odot}$ ,  $R_* = 2 R_{\odot}$ , and  $T_* = 9333 \text{ K}$  – and a flow rate equivalent to the accretion rate onto the star,  $\dot{M} = 7.6 \times 10^{-8} M_{\odot} \text{ yr}^{-1}$  (Garcia Lopez et al. 2006). Based on the CO observations of Isella et al. (2007), we fixed the disk inclination angle to  $i = 44^\circ$  and the major axis position angle to  $133^\circ$  east of north. For this set of fixed parameters, the inner wall is located at a radius of 0.6 AU. There are five remaining free parameters in the model:  $\{\alpha_0, R_c, \epsilon, z_{\text{wall}}, z_{\text{big}}\}$ . To identify a model structure that provides a reasonable match to the HD 163296 observations, we started by comparing synthetic data for a coarse grid of these parameters with the broadband SED. That parameter search was then refined by comparing the model predictions with the observed millimeter continuum visibilities at 271 and 341 GHz. Although not optimized for robust parameter estimation, this approach yielded a template model that exhibits a satisfactory match with these diagnostics of the dust disk. The adopted model has  $\alpha_0 = 0.019$ ,  $R_c = 150 \text{ AU}$ ,  $\epsilon = 0.003$  (the dust-to-gas ratio in the atmosphere is 0.3% of the reference value,  $\zeta_{\text{ref}}$ ), and  $z_{\text{wall}} = 0.1 \text{ AU}$ . The total mass of the model is  $0.089 M_{\odot}$ . All the stellar and disk properties are summarized in Table 3. Figure 5 shows how the value of the  $R_c$  parameter affects the corresponding

continuum visibility profiles at 271 GHz and 341 GHz, the frequencies with the best resolved millimeter continuum data. We find the visibility profiles are matched best with  $R_c$  at 150 AU, a bit larger than 125 AU derived by Hughes et al. (2008) with the similarity solutions.

Figure 6 compares the HD 163296 SED with the models with different values of  $z_{\text{big}}$ , ranging from  $0.5H$  to  $2.5H$ , where  $H$  is the pressure scale height calculated from the local temperature value ( $H = c_s/\Omega$ , where  $c_s$  is the sound speed and  $\Omega$  is the Keplerian angular velocity of the gas. Note that this is merely a convenient scaling, as the vertical structure is solved consistently and does not assume a vertically isothermal profile). The different behaviors of the models are likely caused by the change in the shape of the irradiation surface, which determines the fraction of stellar radiative flux intercepted and reprocessed by the disk. Apparently it is difficult to constrain  $z_{\text{big}}$  from the SED alone due to the complexity of the SED modeling in the mid and far-IR wavelengths. The most substantial discrepancy between the observed SED and the model predictions can be noted in the strength of the 10 and 18  $\mu\text{m}$  silicate emission bands. This might be a reflection that the upper atmosphere layers are hotter than in the model, or that the optical properties of the grains in the atmosphere are slightly different (in size distribution and/or composition) than we assume. The modeling formalism we are using assumes the gas and dust are in thermal equilibrium at all locations in the disk, even in the upper layers of the atmosphere. While that is expected to be a good approximation at the height where most of the stellar radiation is deposited, and where most of the emission from the bands is produced, the gas at larger heights may be even hotter (e.g., Glassgold et al. 2004; Kamp & Dullemond 2004; Jonkheid et al. 2004; Nomura et al. 2007; Gorti & Hollenbach 2008; Woitke et al. 2009; Kamp et al. 2010), which might change the dust density distribution, and hence the silicate emission.

#### 4.2. Stage 2: Refining the Vertical Structure

At the large disk radii probed by our CO observations, the vertical structure of the disk is determined by irradiation. The small dust grains in the disk atmosphere absorb energy from the incident stellar radiation field, and some of that energy is then re-emitted down into the disk interior at longer, infrared wavelengths. Given the increasing densities near the disk midplane, this “external” heating of the disk surface naturally produces a structure with a vertical temperature inversion: the midplane is cooler than the atmosphere (Calvet et al. 1991; Chiang & Goldreich 1997; D’Alessio et al. 1998). In our model prescription for dust settling, the deeper layers in the disk are populated by big dust grains that have low infrared opacities, and therefore are heated less efficiently than their smaller counterparts. Therefore, this concentration of big grains near the disk midplane actually amplifies the temperature

contrast between the surface and interior. In practice, the location of the transition between the small and big grains,  $z_{\text{big}}$ , has a pronounced effect on the vertical temperature gradient (and therefore the vertical density structure). In Figure 7, we demonstrate how  $z_{\text{big}}$  impacts the vertical distributions of temperatures and densities at a fixed radius of 200 AU. A more condensed population of big grains (lower  $z_{\text{big}}$ ) permits more heating at deeper depths into the disk (i.e., lower  $z$ ), producing a warmer disk interior. Likewise, a more vertically extended population of big grains (higher  $z_{\text{big}}$ ) produces much lower temperatures in the disk interior.

The effects of  $z_{\text{big}}$  are difficult to distinguish from the dust tracers alone: the infrared SED and millimeter visibilities do not effectively probe the shape of the vertical temperature profile. However, the CO line emission is expected to be generated in an intermediate disk layer that should be sensitive to this temperature inversion. The main isotope CO lines are optically thick, and therefore excellent temperature diagnostics. By measuring the emission from several CO rotational transitions, their relative strengths may be used to trace the temperature at different depths in the disk (each line probing a layer commensurate with its excitation). Previous analysis of multi-transition CO data have been used to successfully measure the vertical temperature gradient (e.g., Dartois et al. 2003). In this stage of the modeling, we utilized the resolved CO 2–1, 3–2, and 6–5 emission lines toward the HD 163296 disk to determine the value of  $z_{\text{big}}$  that best reproduces the inferred temperature gradient present in its intermediate layer.

To compare the model predictions with the CO data, we first need to fix a set of geometric and kinematic parameters that affect the observed spatio-kinematic behavior of the disk. We assume the disk material orbits the central star in Keplerian motion, and fix the stellar mass and position, and non-thermal turbulent velocity width ( $dV_{\text{turb}}$ ) based on the models of Hughes et al. (2011) and the references noted in §4.1. The effects of inclination ( $i$ ), position angle of the major axis (PA), and systemic velocity ( $V_{\text{lsr}}$ ) are essentially orthogonal to those that depend on the assumed disk structure, and therefore can be optimized independently. All the disk geometric and kinematic parameters are summarized in Table 3. We further assume a simple CO abundance model that depends on the local density and temperature via the parameters introduced by Qi et al. (2008), described below. For a given disk structure and CO abundance model, we use the non-local thermodynamic equilibrium two-dimensional accelerated Monte-Carlo radiative transfer code **RATRAN** to calculate the molecular excitation and generate a sky-projected set of synthetic CO data cubes (Hogerheijde & van der Tak 2000), sampled at the same spatial frequencies as each SMA dataset. The collisional rates are taken from the Leiden Atomic and Molecular Database (Schöier et al. 2005) for non-LTE line radiative transfer calculations. Specifically, in the models used in this paper, we have used the new set of the CO collisional rate coefficients calculated by Yang et al. (2010).

Our adopted abundance model was introduced by Qi et al. (2008), and assumes that the CO emission originates in a vertical layer of the disk with a constant abundance. The upper (surface) and lower (midplane) boundaries of that layer are defined by the parameters  $\sigma_s$  and  $\sigma_m$ , which represent vertically-integrated hydrogen column densities from the disk surface in units of  $1.59 \times 10^{21} \text{ cm}^{-2}$  (the conversion factor of the hydrogen column to  $A_v$  for interstellar dust). The CO abundance ( $f_{\text{CO}}$ ) is assumed to be a constant for the hydrogen column densities from the disk surface  $\sigma_s \geq N \geq \sigma_m$ , with respect to the  $\text{H}_2$  density specified in the disk structure model.

We compute model CO visibilities for a range of disk structure models with different  $z_{\text{big}}$  values, ranging from  $0.5H$ – $3.0H$  in  $0.5H$  steps, where  $H$  is the pressure scale height as we described before. For each  $z_{\text{big}}$  value, we optimized the CO abundance model ( $\sigma_m$ ,  $\sigma_s$  and fractional abundance  $f_{\text{CO}}$ ) to minimize the combined  $\chi^2$  value in reference to the CO J=2–1 and 3–2 visibility data. Because the sensitivity of our CO J=6–5 data is relatively modest, this high-excitation line is better suited to an *a posteriori* check on the fitting results. Nevertheless, the J=6–5 line has a sufficiently high excitation that its luminosity relative to the low-lying J=2–1 and 3–2 lines provides perhaps the best discriminant between different  $z_{\text{big}}$  values. Figure 8 shows the results of this stage of the modeling analysis, marking a direct comparison between the observed and model spectra of the main CO transitions for 3 different  $z_{\text{big}}$  values -  $1.5H$ ,  $2.0H$ , and  $2.5H$ . While any of these models provides a suitable match to both the J=2–1 and 3–2 spectra, only the  $z_{\text{big}} = 2H$  model also matches the J=6–5 line. At  $R=100$  AU of this model, the abundance of big grains has decreased to 50% of its maximum value at a height around 16 AU from the midplane. Figure 9 shows our favored two-dimensional density and temperature distributions for this  $z_{\text{big}} = 2H$  model.

### 4.3. Stage 3: CO Abundance Distributions

We have established a gas+dust structure model that reproduces well the broadband SED, resolved millimeter continuum images, and a multi-transition set of CO spectral images. The next step in the modeling analysis is to constrain the spatial distribution of the CO abundance, relying on the spatially resolved - and more optically thin - CO isotopologue emission, which probe much deeper into the midplane. Here we assume CO and its isotopologues share the same spatial distribution and only differ in fractional abundances. Instead of  $\sigma_m$ , at this stage we adopt the lower boundary (toward midplane) governed by the CO freeze-out temperature,  $T_{\text{CO}}$ , such that  $f_{\text{CO}} \rightarrow 0$  when  $T < T_{\text{CO}}$ , which provides a way of interpreting this lower boundary more physically. For the upper boundary (toward surface), we still adopt  $\sigma_s$  as before.

Using the fixed structure model derived in §4.1 and 4.2, we compute a grid of synthetic  $^{13}\text{CO}$  J=2–1 visibility datasets over a range of  $\sigma_s$ ,  $T_{\text{CO}}$ , and  $f_{^{13}\text{CO}}$  values and compare with the observations. Figure 10 shows the  $\chi^2$  surfaces for the  $^{13}\text{CO}$  J=2–1 emission in the space of these three parameters. We find that the data are best described when  $\sigma_s = 0.79 \pm 0.03$  (i.e., the hydrogen column densities from the disk surface are below  $1.2\text{--}1.3 \times 10^{21} \text{ cm}^{-2}$ ),  $T_{\text{CO}} = 19.0 \pm 0.3 \text{ K}$ , and  $f_{^{13}\text{CO}} = 9.0(\pm 0.6) \times 10^{-7}$ . Figure 9 shows the locations of the CO emission in gray shade on top of the temperature and density profiles (top and middle panels) and the two vertical boundaries ( $\sigma_s = 0.79$  and  $T_{\text{CO}} = 19\text{K}$ ) at  $R = 200 \text{ AU}$  (bottom panel).

Figure 11 shows the effect of the CO freeze-out temperatures  $T_{\text{CO}}$  on the radial column density of  $^{13}\text{CO}$  in the model. Without any freeze-out, the  $^{13}\text{CO}$  column density follows the exponential taper of the  $\text{H}_2$  density profile. The freeze-out at 19 K leads to a significant drop in the gas-phase  $^{13}\text{CO}$  column density beyond a radius of  $\sim 155 \text{ AU}$  (or 310 AU in diameter), which we directly resolve. Even though the  $^{13}\text{CO}$  column densities are different by orders of magnitude, the line emission difference projected to the line-of-sight from the outer disk is very subtle and high spectral resolution data is fundamental for resolving any molecular abundance structure changes at radii beyond  $\sim 155 \text{ AU}$ . Indeed a similar analysis of the  $\text{C}^{18}\text{O}$  J=2–1 emission alone indicates that the data can be fit equally well (or perhaps better) by models that do not include CO freeze-out (i.e. the lower boundary is the midplane,  $z = 0$ ). However, this apparent inconsistency is likely the result of the  $10\times$  lower velocity resolution of the  $\text{C}^{18}\text{O}$  data. Therefore, we don't fit for CO vertical boundaries from the emissions of  $\text{C}^{18}\text{O}$  2–1 and  $\text{C}^{17}\text{O}$  3–2 due to their weaker signals and limited spectral resolutions.

Keeping that resolution effect in mind, we adopt the abundance boundaries derived from the  $^{13}\text{CO}$  2–1 data and then fit the CO,  $\text{C}^{18}\text{O}$ , and  $\text{C}^{17}\text{O}$  data with only the fractional abundances as free parameters. For the  $\sigma_s$  and  $T_{\text{CO}}$  derived above, we find the fractional abundances of CO,  $\text{C}^{18}\text{O}$  and  $\text{C}^{17}\text{O}$  to be  $6.0(\pm 0.3) \times 10^{-5}$ ,  $1.35(\pm 0.20) \times 10^{-7}$  and  $3.5(\pm 1.1) \times 10^{-8}$  respectively, corresponding to  $\text{CO}/^{13}\text{CO} = 67 \pm 8$ ,  $\text{CO}/\text{C}^{18}\text{O} = 444 \pm 88$  and  $\text{CO}/\text{C}^{17}\text{O} = 3.8 \pm 1.7$ . Our derived isotopic ratios are all consistent with the quiescent interstellar gas-phase values, which Wilson (1999) find in the local ISM to be  $\text{CO}/^{13}\text{CO} = 69 \pm 6$ ,  $\text{CO}/\text{C}^{18}\text{O} = 557 \pm 30$ , and  $\text{CO}/\text{C}^{17}\text{O} = 3.6 \pm 0.2$ . Our final model parameters are listed in Table 4. The models are directly compared with the data channel maps in Figures 12 and Figure 13 (with the velocities binned in  $1 \text{ km s}^{-1}$  channels). Table 4 also shows the best-fit fractional abundances in a model of HD 163296 that does not include CO freeze-out; the  $^{13}\text{CO}/\text{C}^{18}\text{O}$  ratio is determined to be  $30.6 \pm 6.1$ , about four times higher than the value  $6.7 \pm 1.4$  derived from our best-fit models that consider CO freeze-out at 19 K (Table 4) or the local ISM value  $8.1 \pm 1.1$  (Wilson 1999). This provides an indirect evidence that we should also take into account CO freeze-out in the  $\text{C}^{18}\text{O}$  2–1 data analysis.

## 5. Discussion

### 5.1. Modeling Dust Emission and CO Line Emission

We have modeled multiple emission lines of CO and its isotopologues from the disk around HD 163296 in the context of an accretion disk model structure, grounded in observations of the broadband SED and resolved millimeter continuum emission. The goal of this modeling effort is to develop a more consistent examination of the connection between the gas and dust phases in the disk. While our modeling framework does not treat the complexity of a completely self-consistent, simultaneous description of the energy balance and chemistry between the gas and dust, it effectively employs a set of parameters that can retrieve molecular abundance information in a way that captures the essential character of the layered disk structures predicted by those more sophisticated models. Most importantly, our approach directly addresses two common issues that are noted in much simpler structure models: (1) a radius (or size) discrepancy between the dust and CO emission, and (2) the degeneracy in the vertical temperature structure for models based solely on the dust emission (i.e., the SED).

A longstanding problem with disk models has been the seemingly different radial distributions of dust and gas when each is considered independently (Dutrey et al. 2007). Isella et al. (2007) presented multi-wavelength millimeter continuum and CO isotopologue observations of the disk around HD 163296 and found a significant discrepancy between the outer radius derived for the dust continuum ( $200 \pm 15$  AU) and that derived from CO emission ( $540 \pm 40$  AU) in their truncated power law models. However, Hughes et al. (2008) showed that models with tapered outer edges can naturally reconcile the apparent size discrepancy in dust and gas millimeter imaging. The successful fitting of CO isotopologues in the HD 163296 disk using the SED-based disk model with an exponentially tapered outer edge, without invoking an unknown or unconstrained chemical effect, provides new support for the necessity of including this feature in outer disk structure.

The SED alone does not provide any direct information on the temperature structure of the intermediate disk layers where the CO (and other molecular) emission is generated. In our modeling framework for the HD 163296 disk, the SED (and millimeter continuum images) can be fit equally well for a wide range of vertical temperature/density profiles, highlighting the degeneracy of the dust data with the parameter  $z_{\text{big}}$ , the height marking the transition between the small grains in the disk atmosphere and the big grains concentrated toward the midplane. However, we have found that resolved observations of optically thick CO lines at a range of excitations can be used to place stringent constraints on the vertical temperature structure. Previous analysis of the CO J=2–1 and 3–2 lines from the HD 163296

disk suggested that gas temperatures were always higher than 20 K, ruling out CO freeze-out as a cause for the depletion of CO abundances (Isella et al. 2007). But as we discussed in §4.2 (see Figure 8), the small excitation leverage between those low-lying transitions is not a strong discriminant of the temperature profile. Here, we make use of the higher-excitation J=6–5 line to better constrain the vertical structure of the disk, and find a colder midplane that is consistent with significant CO freeze-out. Although observations of these various CO transitions is expensive, there are likely other molecules that emit at nearby frequencies and can be used to trace a sufficient range of excitation conditions (e.g., HCO<sup>+</sup>). The essential point is that the temperature structure in the intermediate layers of a disk can only be constrained well using several optically thick emission lines that probe a range of excitation.

## 5.2. The “CO Snow Line”

Theoretical models of the molecular abundances in protoplanetary disks predict three distinct vertical layers (see Bergin et al. 2007). At large heights in the disk atmosphere, temperatures are high and molecular abundances are comparable to those in a standard photon-dominated region (PDR). At intermediate heights, between the midplane and atmosphere, warm temperatures are suitable for high gas-phase abundances of many molecules. And at the deepest layers near the midplane, temperatures are low enough that many molecules are depleted from the gas phase and frozen onto the mantles of dust grains. Aikawa & Nomura (2006) and others, have used this kind of layered physical structure in their chemical reaction network models and shown that CO is expected to be abundant in the warm layer, with  $f_{\text{CO}} \sim 10^{-4}$  almost independent of radius. The boundaries of that layer are defined by the CO freeze-out in the midplane and the photodissociation of CO by high-energy stellar photons in the disk atmosphere. The modeling of the SMA observations of the HD 163296 disk provides direct support for this basic model structure. Our estimate of the upper boundary  $\sigma_s$  is in excellent agreement with models of the upper PDR layer, where CO is photodissociated into its atomic constituents by stellar UV and/or X-ray radiation at column densities  $\lesssim 10^{21} \text{ cm}^{-2}$ <sup>3</sup> (Aikawa & Nomura 2006; Gorti & Hollenbach 2008). The lower boundary that best fits the <sup>13</sup>CO data, corresponding to a temperature of 19 K, is also in excellent agreement with the laboratory studies of CO freeze-out temperature onto dust grains (Collings et al. 2003; Bisschop et al. 2006). The main effect of CO photodesorption (Öberg et al. 2007; Hersant et al. 2009) and other related non-thermal ice desorption mechanisms is to push the

---

<sup>3</sup>A total gas column of  $10^{21} \text{ cm}^{-2}$  corresponds to 1 mag of extinction ( $A_v = 1$ ) at visible wavelengths when the gas-to-dust ratio is 100. But in our model the CO photodissociation front is located at  $A_v \ll 1$  because of the large dust depletion factor as measured with  $\epsilon = 0.003$  in the upper disk layers.

lower boundary to colder temperatures. Since our best-fit CO lower boundary is consistent with thermal desorption, there is no evidence for efficient CO photodesorption in the disk of HD 163296.

Since the term “snow line” is often discussed in planetary formation as some point where the temperature in the midplane would drop below the water ice sublimation level, e.g. in the “minimum-mass solar nebular” model prescribed by Hayashi (1981), we propose to use the term “CO snow line” to indicate where CO freezes out in the disk. It was generally believed that the dust temperature in the disks of Herbig Ae stars is high enough that even the temperature close to the disk midplane is above the temperature of freeze-out of CO (Dutrey et al. 2007; Jonkheid et al. 2007). In this work, the primary line of evidence for CO freeze-out in the disk of HD 163296 comes from the detection of sharp reduction of the effective  $^{13}\text{CO}$  J=2–1 emission area in the outer disk. This is demonstrated in Figure 10 where the  $^{13}\text{CO}$  visibility is best fit with the lower boundary at 19 K, indicating no or very few  $^{13}\text{CO}$  emission from the midplane area below this boundary, as shown in Figure 9. The CO snow line marks drop off at least two orders of magnitude in the column density of  $^{13}\text{CO}$  beyond 155 AU, which is clearly resolved by our interferometric observations. However, the emission lines from CO and its isotopologues are still detectable out to large radii, e.g. >500 AU, which indicates that there are still substantial amount of CO toward surface layer of the outer disk where the temperature is higher than 19 K.

The presence of this CO snow line has a direct impact on some key elements of chemical networks in a disk, especially related to the ionization fraction. The CO abundance is expected to be linearly correlated with the  $\text{HCO}^+$  abundance, but has a strong anti-correlation with  $\text{N}_2\text{H}^+$  since the main destruction pathway for the latter is in reactions with CO (Jørgensen et al. 2004). In the midplane, the depletion of CO beyond the snow line should enhance the deuterated molecular ions,  $\text{H}_2\text{D}^+$ ,  $\text{D}_2\text{H}^+$  and  $\text{D}_3^+$ , such that they become the most abundant ions in the midplane (Ceccarelli & Dominik 2005). So, resolving the CO snow line will eventually help constrain the ionization fraction and the extent of deuterium fractionation in the disk interior.

### 5.3. CO Isotope Ratios

The model developed here indicates that the gas in the intermediate layer of the HD 163296 disk has CO isotopologue abundance ratios that are consistent to those found in the molecular interstellar medium. That finding is in contrast with some previous studies of this and other disks that instead suggested an increasing amount of depletion from  $^{12}\text{CO}$  to  $^{13}\text{CO}$  to  $\text{C}^{18}\text{O}$  (e.g., Isella et al. 2007; Dutrey et al. 1994, 1996). That difference

is likely a manifestation of the underlying modeling approach, as well as the constraining power now available to us from the high-excitation J=6–5 line and the rare isotopologues. When we include CO freeze-out, our models also show no evidence for radial variations of the CO abundance with respect to the H<sub>2</sub> densities inferred (indirectly) from the dust emission. Previous studies have found (much) steeper CO surface density profiles compared to dust (e.g., Pietu et al. 2007, Dutrey et al. 2008). To compare with those findings, we have used an alternative power-law prescription for the radial abundance fractions,  $f_i(r) \propto r^{p_i}$ , and attempted to re-fit our data. The resulting best-fit values of  $p_i$  for <sup>13</sup>CO and C<sup>18</sup>O are  $0.0 \pm 0.1$  and  $0.1 \pm 0.2$ , respectively: both consistent with a radially constant abundance profile. So, when taking into account CO freeze-out at low temperatures, there is no clear evidence that the radial distribution of CO deviates from the underlying total gas surface density. The steep slopes inferred in previous work may be a manifestation of the sharp abundance drop beyond the CO snow line.

This model demonstrates that, given sufficiently strong constraints on the vertical temperature gradient, a unified model of the gas and dust disk can be constructed that conforms to standard ISM-based assumptions about the isotopic abundances and the CO chemistry.

Visser et al. (2009) present a photodissociation model for CO isotopologues including newly updated depth-dependent and isotope-selective photodissociation rates. They find grain growth in circumstellar disks can enhance  $N(^{12}\text{CO})/N(\text{C}^{17}\text{O})$  and  $N(^{12}\text{CO})/N(\text{C}^{18}\text{O})$  ratios by a factor of ten relative to the initial isotopic abundances. We have fit the  $\sigma_s$  and fractional abundances for C<sup>17</sup>O and C<sup>18</sup>O and found that different pairs of  $\sigma_s$  and  $f(\text{C}^{18}\text{O})$  or  $f(\text{C}^{17}\text{O})$  can fit the data equally well, i.e. we can not constrain  $\sigma_s$  due to the limited signal-to-noise ratios of C<sup>18</sup>O J=2–1 and C<sup>17</sup>O 3–2 data. Future observations with greater sensitivity in the CO isotopologues will be essential to investigate the isotope-selective photodissociation on the distributions of CO isotopologues and hence the local isotopic ratios at different layers of the disks.

#### 5.4. Comparison of HD 163296 and TW Hya

In a series of papers, Qi et al. (2004, 2006) modeled the CO J=2–1, 3–2, and 6–5 line emission from the disk around the cooler young star TW Hya. There, the best fit model to the optically thick CO J=2–1 and 3–2 lines tended to underestimate the CO 6–5 emission. To fit all three CO lines simultaneously required additional heating of the disk surface, suggested to be the result of the intense X-ray irradiation field for that source. No such additional heating is required to explain the HD 163296 data. On the contrary, the CO J=6–5 emission required a lower disk interior temperature compared to those predicted by

the typical accretion disk models based on the SED, forcing us to modify the  $z_{\text{big}}$  parameter to fit the data.

There are at least two plausible reasons for the different vertical structures we infer for these disks. First, is the high-energy radiation field from the two stars. *Chandra* X-ray observations reveal a point-like object within  $0''.25$  (30 AU) of HD 163296, with an X-ray luminosity of  $4 \times 10^{29}$  ergs  $\text{s}^{-1}$  (Swartz et al. 2005), about  $5\times$  lower than that from TW Hya (Kastner et al. 1999). Obviously the suggestion that X-ray heating is dependent on the stellar type will require a much larger sample to confirm, as well as more detailed radiative transfer modeling of the high-energy heating of these disks. However, it is an exciting prospect that the interior structures of these disks may be very different depending on the connection between the stellar mass and the irradiation environment, with implications both for disk evolution and chemistry. A second possibility may lie with the level of turbulence in these disks. In our model, the vertical structure is governed by the settling of large dust grains. The timescale for gravitational sedimentation is expected to be short, with big grains reaching the midplane in less than  $\sim 1$  Myr (Dullemond & Dominik 2004) unless the dust is effectively stirred up by turbulence. The more vertically extended population of big grains required to model the HD 163296 disk might be commensurate with more efficient stirring, or rather inhibited settling. Hughes et al. (2011) suggest a  $300 \text{ m s}^{-1}$  turbulent linewidth in the CO layer of the HD 163296 disk, much larger than the  $\lesssim 40 \text{ m s}^{-1}$  they find for the TW Hya disk. Perhaps turbulent stirring is responsible for lofting the big grains above the midplane in the HD 163296 disk, enhancing the radiative cooling.

## 6. Summary

We present CO line and dust emission observations of the disk around the Herbig Ae star HD 163296 and develop a model framework that describes in a consistent way the spectral energy distribution, resolved millimeter dust continuum data, and multiple emission lines of CO and its isotopologues. The fitting results support the general picture of CO vertical distribution regulated by photodissociation at a surface where the hydrogen column density is  $\lesssim 10^{21} \text{ cm}^{-2}$  and by CO freeze-out at depths below 20 K in the midplane. The main conclusions are summarized here:

1. We confirm a tapered exponential edge in the surface density distribution, an outcome of the similarity solution of the time evolution of accretion disks, can account for the size discrepancy in dust continuum and CO emission (Hughes et al. 2008). This means that constraints from dust modeling can be applied to CO gas modeling, significantly reducing the number of free parameters.

2. We find in the disk model the transition between the “small” and “big” dust grain populations,  $z = z_{\text{big}}$  in units of the gas scale height  $H$ , regulates the vertical temperature and density profiles between the disk midplane and surface. Multiple transitions of CO, especially the CO 6-5 line, which requires much higher excitation, can be used to constrain the location of  $z_{\text{big}}$ , thus the temperature structure in the disk intermediate layer. We find the resulting disk model for HD 163296 has a cold midplane populated by large grains with a large scale height ( $z_{\text{big}} = 2H$ ). Since the vertical temperature in the HD 163296 disk is governed mainly by the settling, or lack of settling, of large grains, a possible explanation for the relatively cold interior of HD 163296 disk may be a high level of gas turbulence (see Hughes et al. 2011).
3. Using the model with temperature structure constrained by the CO multi-transition analysis, we fit for the location of emission from  $^{13}\text{CO}$  and constrain the vertical distribution of the emission region to lie between a lower boundary set by the temperature where CO freezes out onto dust grains (at heights where  $T \lesssim 19$  K) and an upper boundary where densities are low enough that stellar and interstellar radiation can photodissociate the CO molecule (where the vertically integrated hydrogen column density from the disk surface is  $\lesssim 10^{21} \text{ cm}^{-2}$ ). The CO freeze-out produces a significant drop in the gas-phase CO column density beyond a radius of about 155 AU, effectively a CO snow line that is resolved directly by the observations. The CO depletion, generally found in disks, can be successfully accounted for considering both the CO freeze-out and photodissociation.
4. Taking the CO freeze-out into consideration in the disk model and assuming CO isotopologues sharing the same spatial distribution, the isotopic ratios of  $^{12}\text{C}/^{13}\text{C}$ ,  $^{16}\text{O}/^{18}\text{O}$  and  $^{18}\text{O}/^{17}\text{O}$  are consistent with the standard quiescent interstellar gas-phase values and show no evidence for unusual fractionation. More sensitive data is needed to investigate the distribution differences among those CO isotopologues and the local isotopic ratios at different layers of the disks.

This detailed investigation of the HD 163296 disk demonstrates the potential of a staged, parametric technique for constructing unified gas and dust structure models and constraining the distribution of molecular abundances using resolved multi-transition, multi-isotope observations. The analysis provides the essential framework for more general observational studies of molecular line emission in protoplanetary disks.

We thank Edwin Bergin, Eugene Chiang and Jeremy Drake for beneficial conversations, and a referee for constructive comments on the paper. Support for K. I. O. is provided by NASA through a Hubble Fellowship grant awarded by the Space Telescope Science Institute,

which is operated by the Association of Universities for Research in Astronomy, Inc., for NASA, under contract NAS 5-26555. Support for A. M. H. is provided by a fellowship from the Miller Institute for Basic Research in Science. We acknowledge NASA Origins of Solar Systems grant No. NNX11AK63G.

## REFERENCES

- Acke, B., & van den Ancker, M. E. 2004, *A&A*, 426, 151
- Aikawa, Y. 2007, *ApJ*, 656, L93
- Aikawa, Y., Miyama, S. M., Nakano, T., & Umebayashi, T. 1996, *ApJ*, 467, 684
- Aikawa, Y., & Nomura, H. 2006, *ApJ*, 642, 1152
- Andrews, S. M., Wilner, D. J., Hughes, A. M., Qi, C., & Dullemond, C. P. 2009, *ApJ*, 700, 1502
- . 2010, *ApJ*, 723, 1241
- Beichman, C. A., Neugebauer, G., Habing, H. J., Clegg, P. E., & Chester, T. J., eds. 1988, *Infrared astronomical satellite (IRAS) catalogs and atlases. Volume 1: Explanatory supplement, Vol. 1*
- Bergin, E. A., Aikawa, Y., Blake, G. A., & van Dishoeck, E. F. 2007, in *Protostars and Planets V*, ed. B. Reipurth, D. Jewitt, & K. Keil, 751–766
- Berrilli, F., Corciulo, G., Ingrassio, G., Lorenzetti, D., Nisini, B., & Strafella, F. 1992, *ApJ*, 398, 254
- Bisschop, S. E., Fraser, H. J., Öberg, K. I., van Dishoeck, E. F., & Schlemmer, S. 2006, *A&A*, 449, 1297
- Bruzual A., G., & Charlot, S. 1993, *ApJ*, 405, 538
- Calvet, N., Patino, A., Magris, G. C., & D’Alessio, P. 1991, *ApJ*, 380, 617
- Ceccarelli, C., & Dominik, C. 2005, *A&A*, 440, 583
- Chiang, E. I., & Goldreich, P. 1997, *ApJ*, 490, 368
- Collings, M. P., Dever, J. W., Fraser, H. J., McCoustra, M. R. S., & Williams, D. A. 2003, *ApJ*, 583, 1058

- Cutri, R. M., et al. 2003, VizieR Online Data Catalog, 2246, 0
- D’Alessio, P., Calvet, N., & Hartmann, L. 2001, ApJ, 553, 321
- D’Alessio, P., Calvet, N., Hartmann, L., Franco-Hernández, R., & Servín, H. 2006, ApJ, 638, 314
- D’Alessio, P., Calvet, N., Hartmann, L., Lizano, S., & Cantó, J. 1999, ApJ, 527, 893
- D’Alessio, P., Canto, J., Calvet, N., & Lizano, S. 1998, ApJ, 500, 411
- D’Alessio, P., et al. 2005, ApJ, 621, 461
- Dartois, E., Dutrey, A., & Guilloteau, S. 2003, A&A, 399, 773
- Devine, D., Grady, C. A., Kimble, R. A., Woodgate, B., Palunas, P., & Linsky, J. L. 2000, in American Astronomical Society Meeting, Vol. 197, 0809+
- Draine, B. T., & Lee, H. M. 1984, ApJ, 285, 89
- Dullemond, C. P., & Dominik, C. 2004, A&A, 421, 1075
- Dullemond, C. P., Dominik, C., & Natta, A. 2001, ApJ, 560, 957
- Dutrey, A., Guilloteau, S., Duvert, G., Prato, L., Simon, M., Schuster, K., & Menard, F. 1996, A&A, 309, 493
- Dutrey, A., Guilloteau, S., & Guelin, M. 1997, A&A, 317, L55
- Dutrey, A., Guilloteau, S., & Ho, P. 2007, in Protostars and Planets V, ed. B. Reipurth, D. Jewitt, & K. Keil, 495–506
- Dutrey, A., Guilloteau, S., & Simon, M. 1994, A&A, 286, 149
- Eiroa, C., et al. 2001, A&A, 365, 110
- Garcia Lopez, R., Natta, A., Testi, L., & Habart, E. 2006, A&A, 459, 837
- Glassgold, A. E., Najita, J., & Igea, J. 2004, ApJ, 615, 972
- Gorti, U., & Hollenbach, D. 2008, ApJ, 683, 287
- Grady, C. A., et al. 2000, ApJ, 544, 895
- Hartmann, L., Calvet, N., Gullbring, E., & D’Alessio, P. 1998, ApJ, 495, 385

- Hayashi, C. 1981, *Progress of Theoretical Physics Supplement*, 70, 35
- Hersant, F., Wakelam, V., Dutrey, A., Guilloteau, S., & Herbst, E. 2009, *A&A*, 493, L49
- Hillenbrand, L. A., Strom, S. E., Vrba, F. J., & Keene, J. 1992, *ApJ*, 397, 613
- Hogerheijde, M. R., & van der Tak, F. F. S. 2000, *A&A*, 362, 697
- Hughes, A. M., Wilner, D. J., Andrews, S. M., Qi, C., & Hogerheijde, M. R. 2011, *ApJ*, 727, 85
- Hughes, A. M., Wilner, D. J., Qi, C., & Hogerheijde, M. R. 2008, *ApJ*, 678, 1119
- Isella, A., Testi, L., Natta, A., Neri, R., Wilner, D., & Qi, C. 2007, *A&A*, 469, 213
- Jayawardhana, R., Fisher, R. S., Telesco, C. M., Piña, R. K., Barrado y Navascués, D., Hartmann, L. W., & Fazio, G. G. 2001, *AJ*, 122, 2047
- Jonkheid, B., Dullemond, C. P., Hogerheijde, M. R., & van Dishoeck, E. F. 2007, *A&A*, 463, 203
- Jonkheid, B., Faas, F. G. A., van Zadelhoff, G.-J., & van Dishoeck, E. F. 2004, *A&A*, 428, 511
- Jørgensen, J. K., Schöier, F. L., & van Dishoeck, E. F. 2004, *A&A*, 416, 603
- Kamp, I., & Dullemond, C. P. 2004, *ApJ*, 615, 991
- Kamp, I., Tilling, I., Woitke, P., Thi, W., & Hogerheijde, M. 2010, *A&A*, 510, A18+
- Kastner, J. H., Huenemoerder, D. P., Schulz, N. S., & Weintraub, D. A. 1999, *ApJ*, 525, 837
- Malfait, K., Bogaert, E., & Waelkens, C. 1998, *A&A*, 331, 211
- Mannings, V., & Sargent, A. I. 1997, *ApJ*, 490, 792
- Muzerolle, J., D'Alessio, P., Calvet, N., & Hartmann, L. 2004, *ApJ*, 617, 406
- Natta, A., Grinin, V., & Mannings, V. 2000, *Protostars and Planets IV*, 559
- Natta, A., Testi, L., Neri, R., Shepherd, D. S., & Wilner, D. J. 2004, *A&A*, 416, 179
- Nomura, H., Aikawa, Y., Tsujimoto, M., Nakagawa, Y., & Millar, T. J. 2007, *ApJ*, 661, 334
- Öberg, K. I., Fuchs, G. W., Awad, Z., Fraser, H. J., Schlemmer, S., van Dishoeck, E. F., & Linnartz, H. 2007, *ApJ*, 662, L23

- Oudmaijer, R. D., et al. 2001, *A&A*, 379, 564
- Perryman, M. A. C., et al. 1997, *A&A*, 323, L49
- Piétu, V., Dutrey, A., & Guilloteau, S. 2007, *A&A*, 467, 163
- Qi, C. 2001, PhD thesis, California Institute of Technology
- Qi, C., Wilner, D. J., Aikawa, Y., Blake, G. A., & Hogerheijde, M. R. 2008, *ApJ*, 681, 1396
- Qi, C., Wilner, D. J., Calvet, N., Bourke, T. L., Blake, G. A., Hogerheijde, M. R., Ho, P. T. P., & Bergin, E. 2006, *ApJ*, 636, L157
- Qi, C., et al. 2004, *ApJ*, 616, L11
- Schöier, F. L., van der Tak, F. F. S., van Dishoeck, E. F., & Black, J. H. 2005, *A&A*, 432, 369
- Shakura, N. I., & Sunyaev, R. A. 1973, *A&A*, 24, 337
- Swartz, D. A., Drake, J. J., Elsner, R. F., Ghosh, K. K., Grady, C. A., Wassell, E., Woodgate, B. E., & Kimble, R. A. 2005, *ApJ*, 628, 811
- Tannirkulam, A., et al. 2008, *ApJ*, 689, 513
- Thi, W.-F., van Zadelhoff, G.-J., & van Dishoeck, E. F. 2004, *A&A*, 425, 955
- Thi, W. F., et al. 2001, *ApJ*, 561, 1074
- Visser, R., van Dishoeck, E. F., & Black, J. H. 2009, *A&A*, 503, 323
- van den Ancker, M. E., de Winter, D., & Tjin A Djie, H. R. E. 1998, *A&A*, 330, 145
- van Zadelhoff, G.-J., van Dishoeck, E. F., Thi, W.-F., & Blake, G. A. 2001, *A&A*, 377, 566
- Wassell, E. J., Grady, C. A., Woodgate, B., Kimble, R. A., & Bruhweiler, F. C. 2006, *ApJ*, 650, 985
- Wilson, T. L. 1999, *Reports on Progress in Physics*, 62, 143
- Woitke, P., Kamp, I., & Thi, W.-F. 2009, *A&A*, 501, 383
- Yang, B., Stancil, P. C., Balakrishnan, N., & Forrey, R. C. 2010, *ApJ*, 718, 1062

Table 1. Observational parameters for SMA HD 163296 observations

Parameters	CO 2–1	CO 3–2 <sup>b</sup>	CO 6–5	<sup>13</sup> CO 2–1	C <sup>18</sup> O 2–1	C <sup>17</sup> O 3–2
Rest Frequency (GHz):	230.53800	345.79599	691.47308	220.39868	219.56036	337.06113
Observations <sup>a</sup>	2010 May 17 (C) 2010 Sep 14 (E)	2009 May 6 (C) 2009 Aug 22(E)	2007 Mar 20 (C)	2010 May 15 (C) 2010 Sep 11 (E)	2010 May 15 (C) 2010 Sep 11 (E)	2005 Aug 23 (C)
Tsys	93–207	147–273	1368–4764	82–146	82–146	210–603
Baselines	6–151	10–146	23–158	6–145	6–145	8–80
Spectral resolution (km s <sup>-1</sup> ):	0.066	0.044	0.88	0.069	0.55	0.72

<sup>a</sup>C: compact configuration; E: extended configuration.

<sup>b</sup>Observational parameters from Hughes et al. (2011)

Table 2. Continuum and emission line results

$\lambda(\text{mm})$	Beam	PA	Flux (Jy)
1.36	$3''.5 \times 2''.2$	$55.8^\circ$	$0.615 \pm 0.004$
1.33	$4''.7 \times 2''.8$	$24.2^\circ$	$0.670 \pm 0.007$
1.11	$3''.0 \times 1''.9$	$57.8^\circ$	$1.039 \pm 0.007$
0.88	$1''.8 \times 1''.3$	$47.6^\circ$	$1.74 \pm 0.12$
0.44	$2''.7 \times 2''.2$	$-6.9^\circ$	$7.5 \pm 0.5$
Transitions	Beam	PA	Integrated Intensity <sup>b</sup> (Jy km <sup>-1</sup> )
CO 2–1	$2''.1 \times 1''.8$	$10.5^\circ$	$54.17 \pm 0.39$
CO 3–2	$1''.7 \times 1''.3$	$46.7^\circ$	$98.72 \pm 1.69$
CO 6–5	$2''.7 \times 1''.4$	$1.8^\circ$	$58.66 \pm 6.44$
<sup>13</sup> CO 2–1	$1''.9 \times 1''.8$	$5.5^\circ$	$18.76 \pm 0.24$
C <sup>18</sup> O 2–1	$1''.9 \times 1''.8$	$5.5^\circ$	$6.30 \pm 0.16$
C <sup>17</sup> O 3–2	$3''.2 \times 2''.2$	$13.1^\circ$	$11.64 \pm 0.76$

<sup>a</sup>Intensity averaged over the whole emission area.

Table 3. Physical model for the disk of HD 163296

Parameters	Values
Stellar and accretion properties	
Spectral type	A1
Effective temperature: $T_*$ (K)	9333
Visual extinction: $A_v$	0.3
Estimated distance: d(pc)	122
Stellar radius: $R_*(R_\odot)$	2
Stellar mass: $M_*(M_\odot)$	2.3
Accretion rate: $\dot{M}(M_\odot \text{ yr}^{-1})$	$7.6 \times 10^{-8}$
Disk structure properties	
Disk mass: $M_d(M_\odot)$	0.089
Characteristic radius: $R_c(\text{AU})$	150
Viscosity coefficient: $\alpha_0$	0.019
Depletion factor of the atmospheric small grains: $\epsilon^a$	0.003
$z_{\text{big}}^a (H^b)$	2.0
Inner wall radius: $R_{\text{wall}}(\text{AU})$	0.6
Inner wall scale height: $z_{\text{wall}}(\text{AU})$	0.1
Disk geometric and kinematic properties	
Inclination: $i(\text{deg})$	$44 \pm 2$
Systemic velocity: $V_{LSR}(\text{km s}^{-1})$	$5.8 \pm 0.2$
Turbulent line width <sup>c</sup> : $v_{\text{turb}}(\text{km s}^{-1})$	0.2
Position angle: P.A.(deg)	$133 \pm 3$

<sup>a</sup>See definition in paper or D’Alessio et al. (2006).

<sup>b</sup>Gas scale height.

<sup>c</sup>Fixed parameter.

Table 4. Fitting results: fractional abundances and distributions

Parameters	CO 2–1 & 3–2	<sup>13</sup> CO 2–1	C <sup>18</sup> O 2–1	C <sup>17</sup> O 3–2
Midplane freeze-out temperature (K)	19.0*	19.0 ± 0.3	19.0*	19.0*
$\sigma_s$	0.79*	0.79 ± 0.03	0.79*	0.79*
Fractional abundance	$(6.0 \pm 0.3) \times 10^{-5}$	$(9.0 \pm 0.6) \times 10^{-7}$	$(1.35 \pm 0.20) \times 10^{-7}$	$(3.5 \pm 1.1) \times 10^{-8}$
Fractional abundance (no freeze-out)	$(6.5 \pm 0.3) \times 10^{-5}$	$(4.6 \pm 0.3) \times 10^{-7}$	$(1.5 \pm 0.2) \times 10^{-8}$	$(7.0 \pm 2.2) \times 10^{-8}$

\*Parameter values adopted from <sup>13</sup>CO 2–1 fitting.

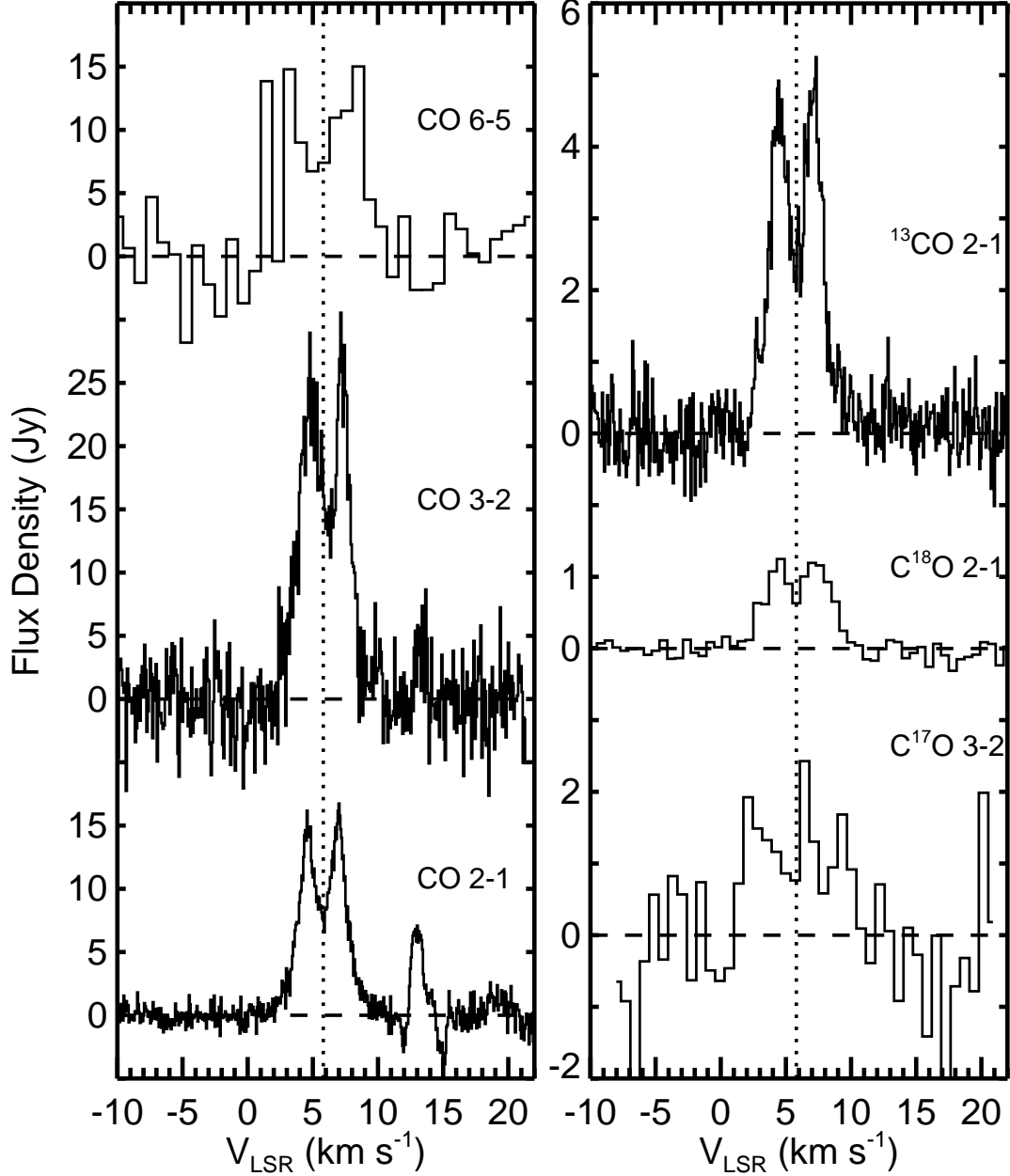


Fig. 1.— Spatially integrated spectra at the peak continuum (stellar) position of HD 163296. The fluxes are averaged over the emission areas ( $4''$  box for CO 6–5;  $10''$  box for other lines). The vertical dotted line indicates the position of the fitted  $V_{LSR}$ .

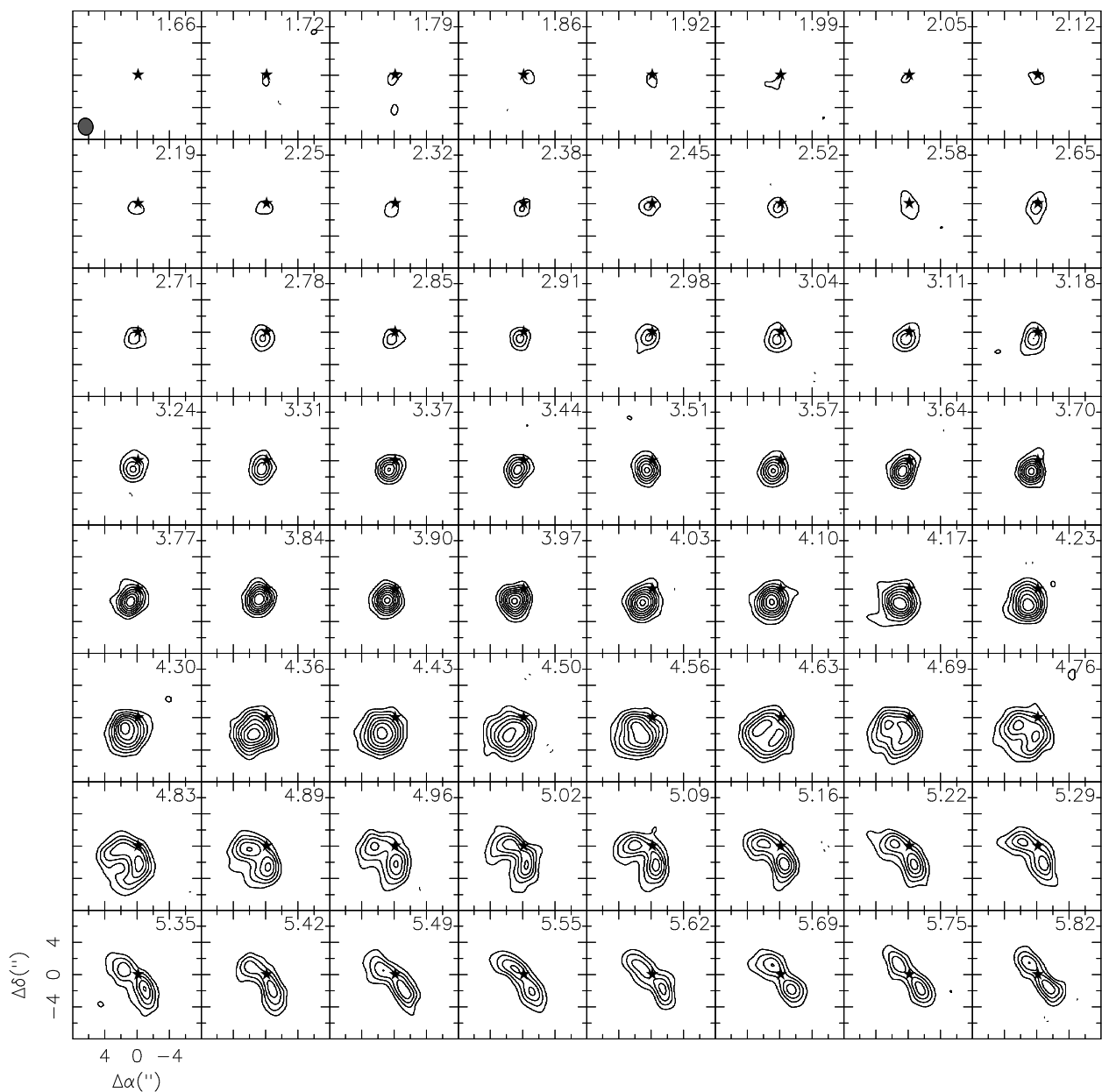
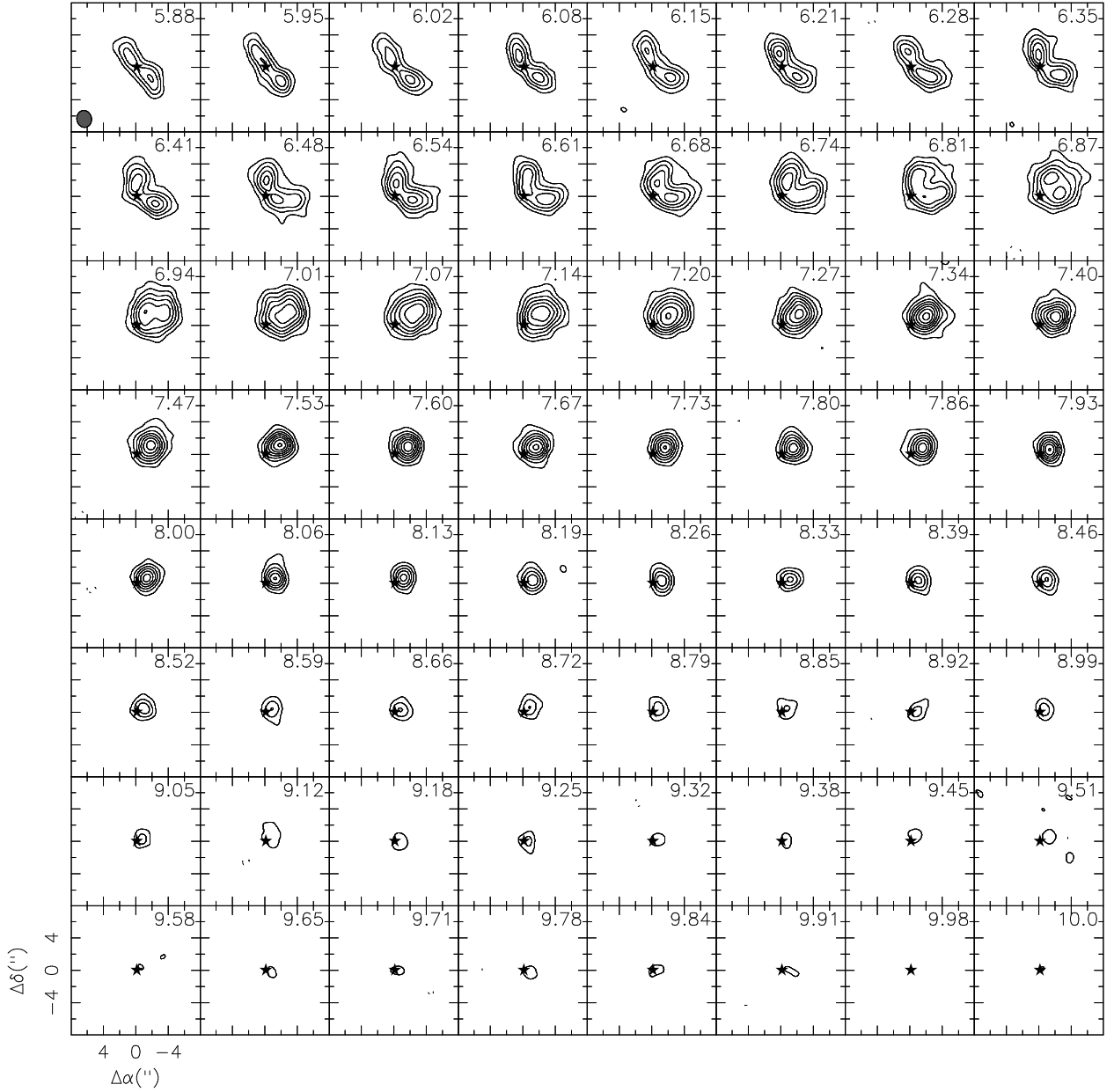


Fig. 2.— Channel maps of the CO J=2-1 line emission from the disk around HD 163296. The LSR velocity is indicated in the upper right of each channel, while the synthesized beam size and orientation ( $2''.1 \times 1''.8$  at a position angle of  $10.5^\circ$ ) is indicated in the upper left panel. The contours are  $0.18 \text{ Jy Beam}^{-1} (1\sigma) \times [3, 6, 9, 12, 15, 18, 21, 24, 27]$ . The star symbol indicates the disk center.



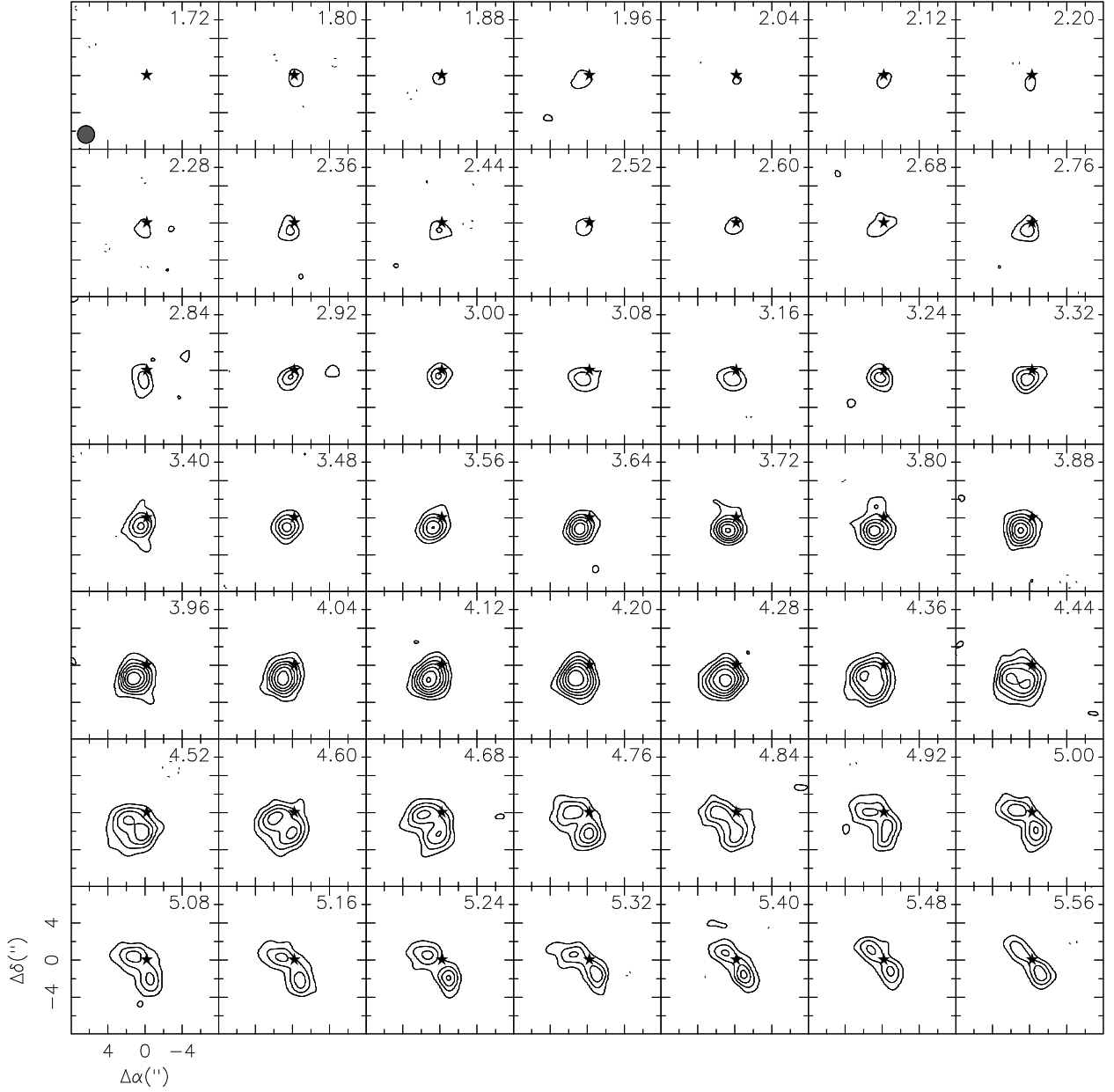
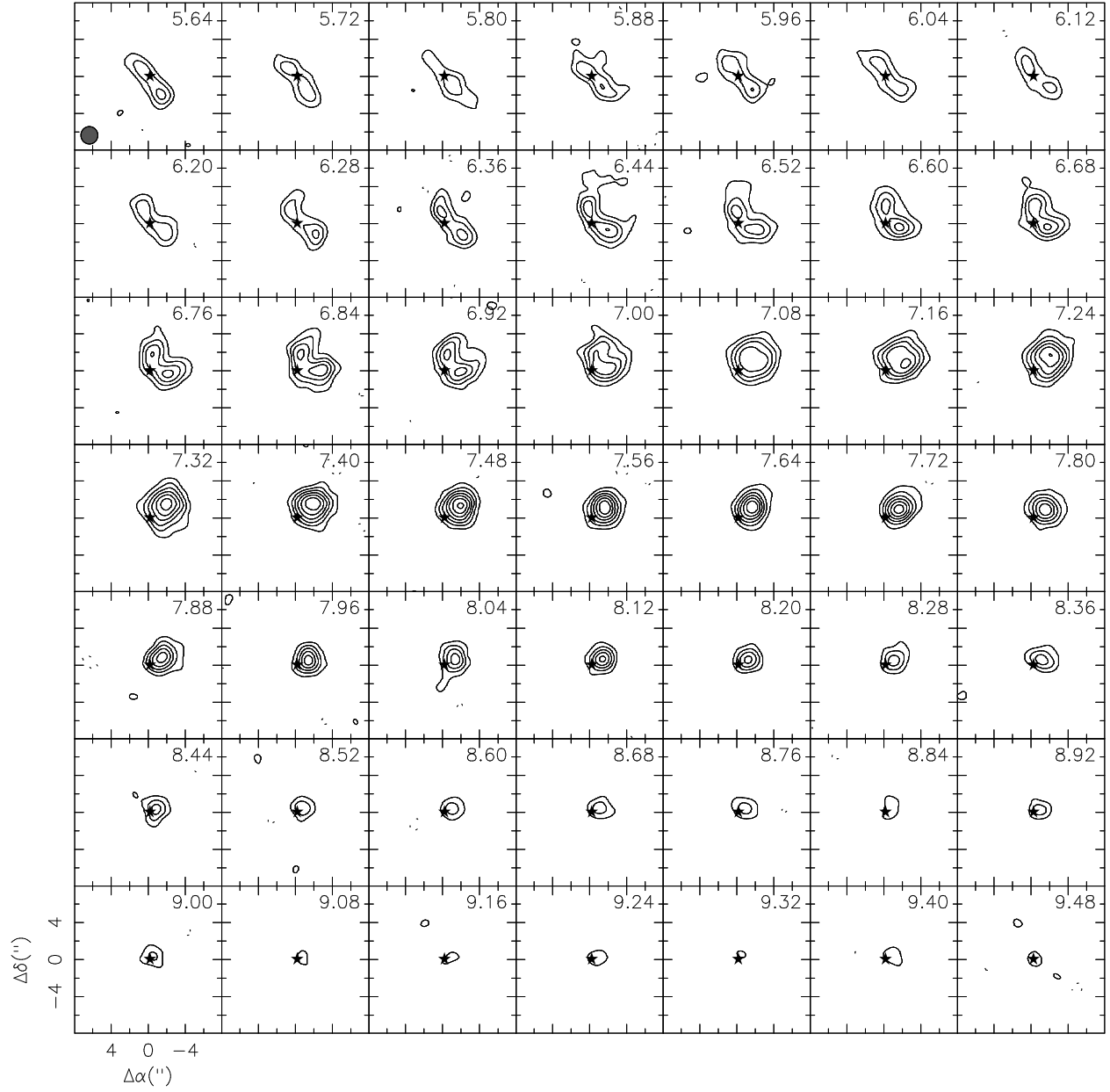


Fig. 3.— Same as Figure 2, but for  $^{13}\text{CO}$  2–1. The beam size is  $1''.9 \times 1''.8$  at a position angle of  $5.5^\circ$  and the contours are  $0.08 \text{ Jy Beam}^{-1} (1\sigma) \times [3, 6, 9, 12, 15, 18, 21, 24]$ .



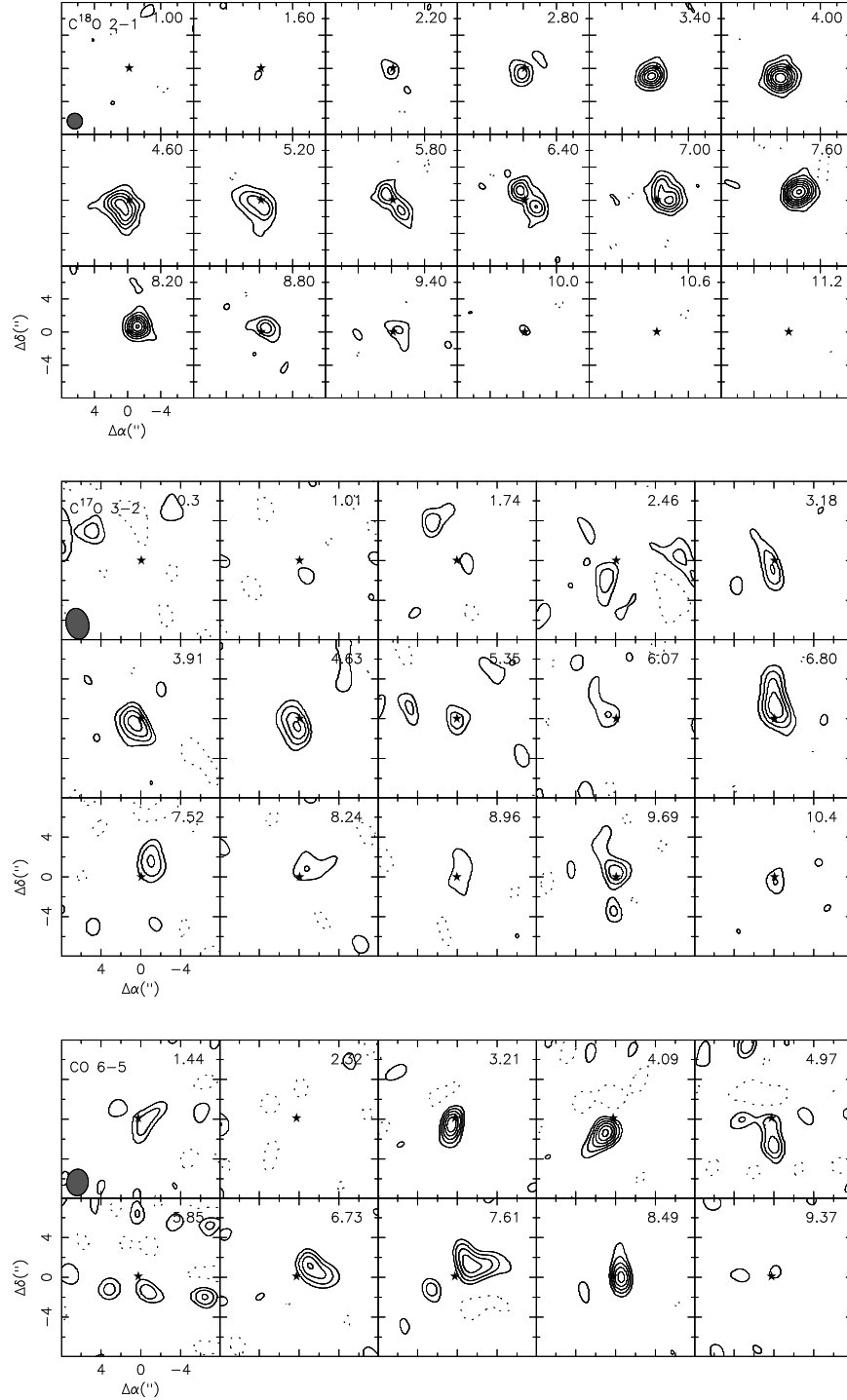


Fig. 4.— Same as Figure 2, but for  $\text{C}^{18}\text{O}$  2–1,  $\text{C}^{17}\text{O}$  3–2 and CO 6–5. For  $\text{C}^{18}\text{O}$  2–1, the beam size is  $1''.9 \times 1''.8$  at a position angle of  $5.5^\circ$  and the contours are  $0.025 \text{ Jy Beam}^{-1}$  ( $1\sigma$ )  $\times [3, 6, 9, 12, 15, 18, 21, 24]$ ; for  $\text{C}^{17}\text{O}$  3–2, the beam size is  $3''.1 \times 2''.3$  at a position angle of  $12.8^\circ$  and the contours are  $0.2 \text{ Jy Beam}^{-1}$  ( $1\sigma$ )  $\times [2, 3, 4, 5]$ ; for CO 6–5, the beam size is  $2''.7 \times 2''.2$  at a position angle of  $-5.6^\circ$  and the contours are  $3.0 \text{ Jy Beam}^{-1}$  ( $1\sigma$ )  $\times [2, 3, 4, 5, 6, 7]$ .

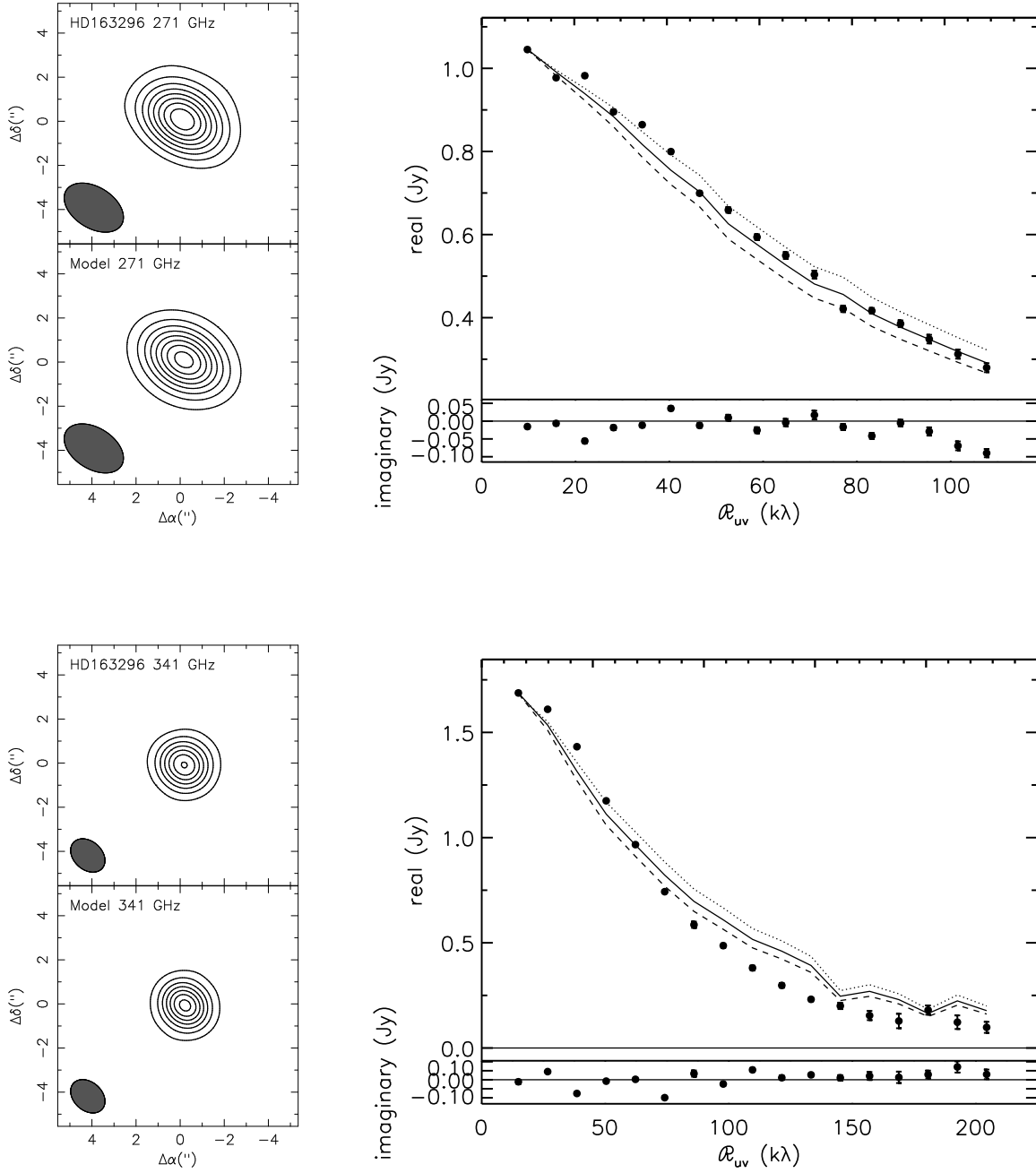


Fig. 5.— *Top panels* (Left): The predicted continuum image vs data at 271 GHz. Contours are shown at  $3\sigma$  intervals. (Right): The predicted 271 GHz continuum visibility profiles for Models with  $R_c=125$  AU(dotted line), 150 AU(solid line), 175 AU(dashed line). *Bottom panels*: The predicted continuum image and visibilities vs data at 341 GHz.

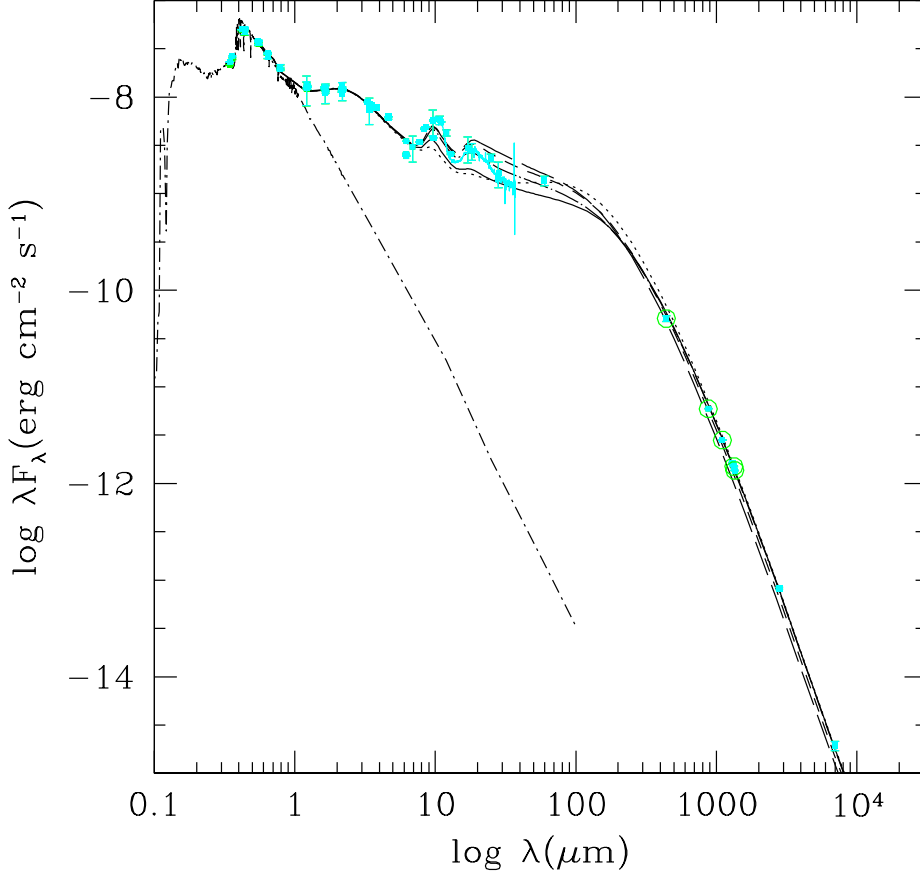


Fig. 6.— The HD 163296 SED. Optical and infrared bands: UBVJHKLM from Malfait et al. (1998); UBVRI from Hillenbrand et al. (1992); BV from Oudmaijer et al. (2001); BVRIJHK from Tannirkulam et al. (2008); JHKLM and 8–13  $\mu\text{mm}$  bands from Berrilli et al. (1992); JHK from Eiroa et al. (2001) and 2MASS (Cutri et al. 2003); ISO spectra (Acke & van den Ancker 2004; Thi et al. 2001); the CTIO and Keck telescopes data (Jayawardhana et al. 2001); IRAS (Beichman et al. 1988); Spitzer-IRS (retrieved from Spitzer archive website: irsa.ipac.caltech.edu). Millimeter fluxes are from this paper (marked with circles) and Isella et al. (2007). Overlaid on the SED are the models which have:  $\dot{M} = 7.6 \times 10^{-8} M_\odot/\text{yr}$ ,  $\alpha_0 = 0.019$ ,  $\epsilon = 0.003$ ,  $R_c = 150$  AU,  $\cos i = 0.72$ , a vertical wall at the dust sublimation radius, calculated assuming  $T_{\text{sub}} = 1500$  K, with  $R_{\text{wall}} = 0.6$  AU and a height  $z_{\text{wall}} = 0.17R_{\text{wall}}$ . The stellar photosphere (the short-long-dashed line) is from the library for population synthesis from Bruzual A. & Charlot (1993). The model SED lines are laid out for models with different values of  $z_{\text{big}}/H = 0.5$ (long-dashed), 1.0(short-dashed), 1.5(dot-dashed), 2.0(solid) and 2.5 (dotted).

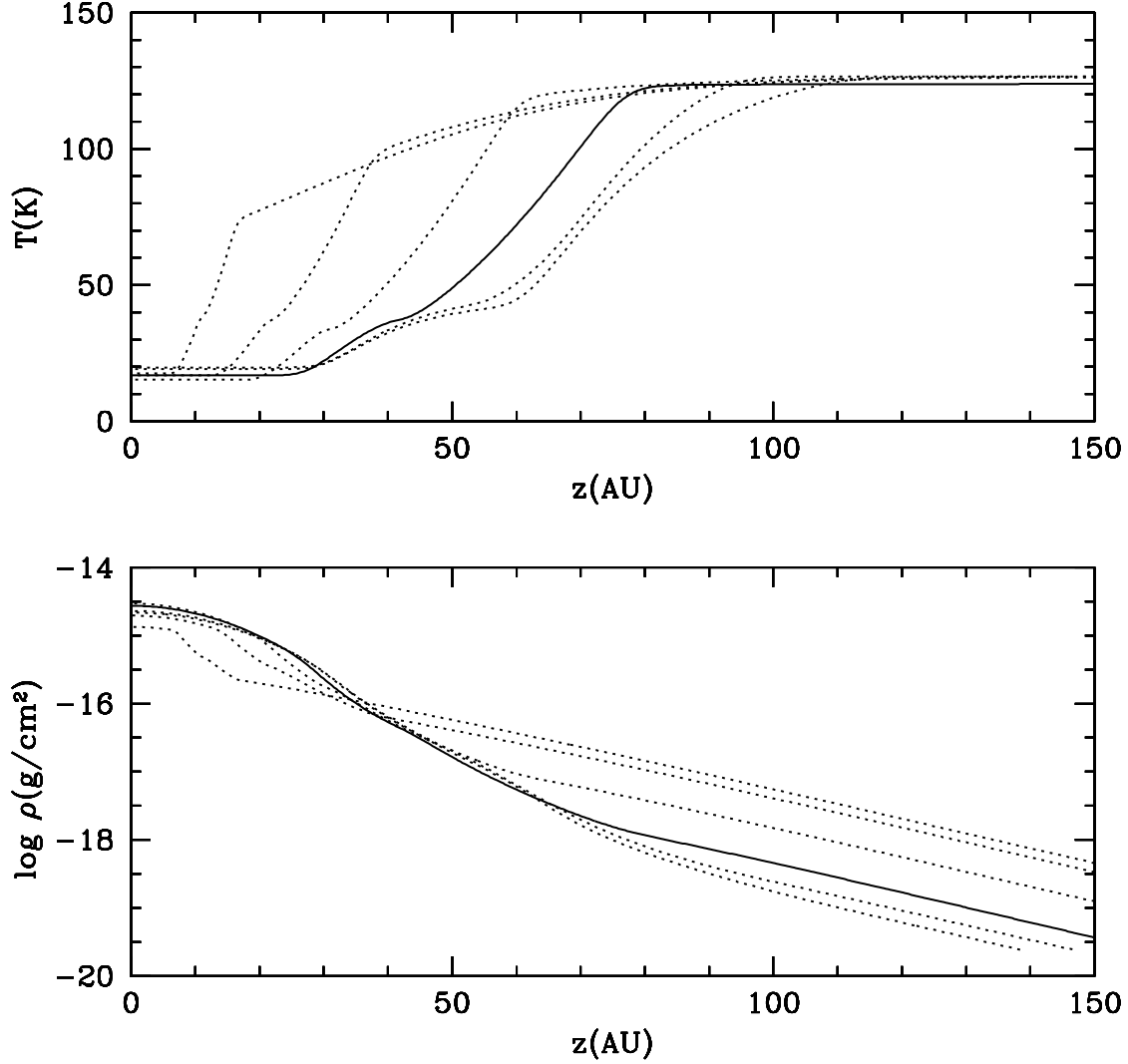


Fig. 7.— Upper panel: Temperature vs height at  $R = 200$  AU for disk models with  $\dot{M} = 7.6 \times 10^{-8} M_{\odot}/\text{yr}$ ,  $\alpha_0 = 0.019$ ,  $\epsilon = 0.003$ ,  $R_c = 150$  AU, and different values of  $z_{\text{big}}/H = 0.5, 1, 1.5, 2.0, 2.5, 3$  (from left to right). The fiducial model, with  $z_{\text{big}} = 2H$  is showed with a solid line. Lower panel: Density vs height at  $R = 200$  AU for the same models. The lines are laid out from top to bottom for models with different values of  $z_{\text{big}}/H = 0.5, 1, 1.5, 2.0, 2.5, 3$  at  $z > 100$  AU.

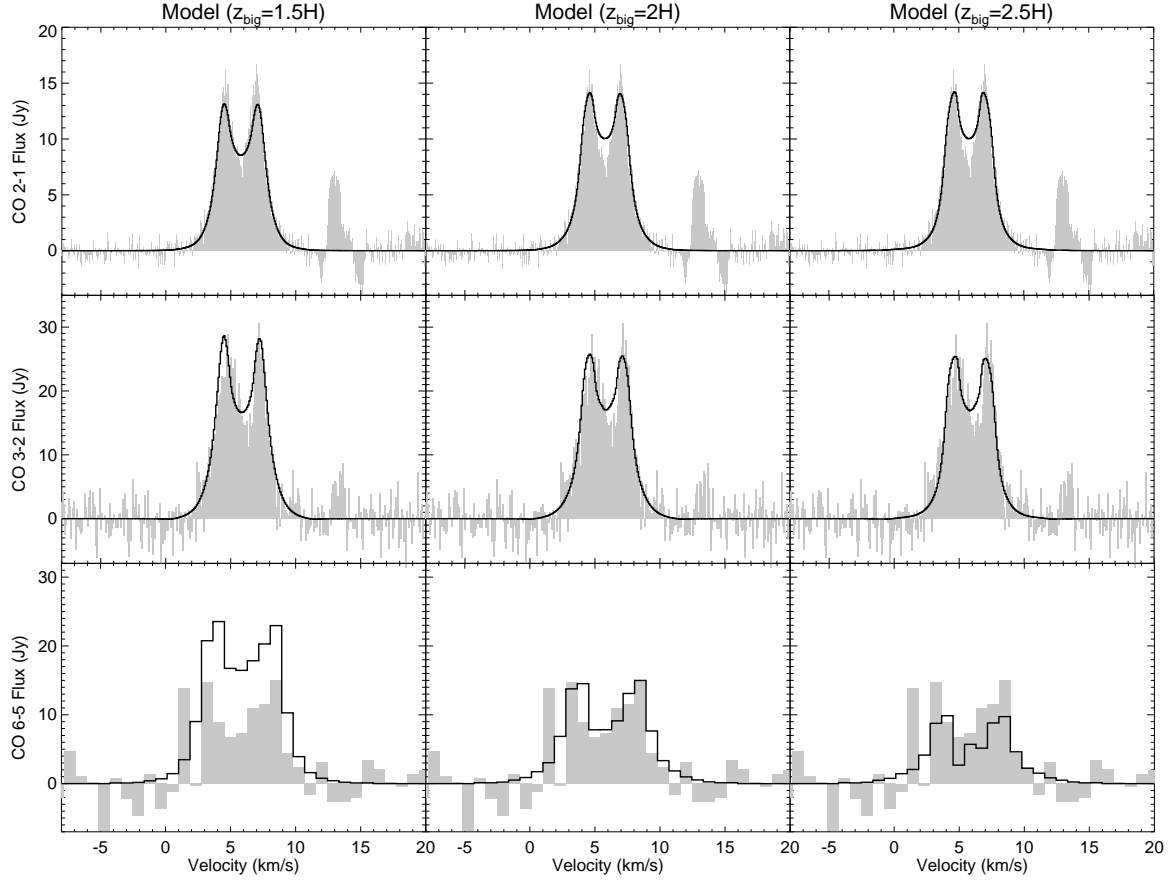


Fig. 8.— CO J=2–1, 3–2, and 6–5 model spectra (black lines) overlaid with the HD 163296 spectra in grey shade. The left, middle and right column are the simulated models with  $z_{\text{big}}/H = 1.5, 2.0, 2.5$ . Note that all the models have been sampled at the same spatial frequencies as each SMA dataset.

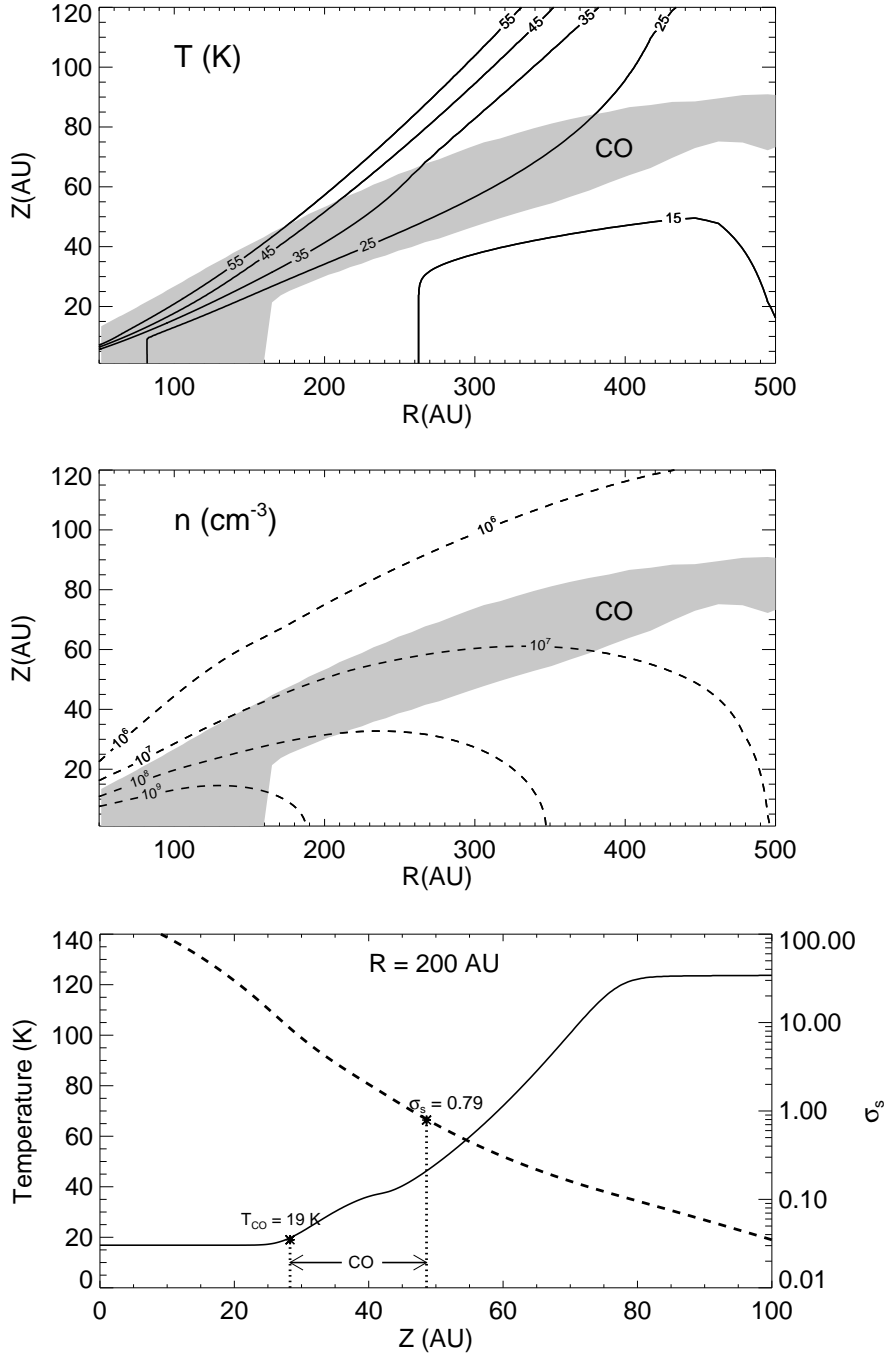


Fig. 9.— The irradiated accretion disk structure model for HD 163296 with  $z_{\text{big}}/H = 2.0$  and  $R_c=150$  AU. *Top and middle panels:* Temperature and density profiles are indicated by solid and dashed lines, respectively. The CO emission area constrained by the best-fit vertical boundaries is shown in grey shade. *Bottom panel:* The vertical distributions of temperature and  $\sigma_s$  at  $R = 200$  AU are indicated by solid and dashed lines, respectively. The vertical dotted lines show the best-fit locations of the lower boundary ( $T_{\text{CO}} = 19$  K) and upper boundary ( $\sigma_s=0.79$ ) for CO.

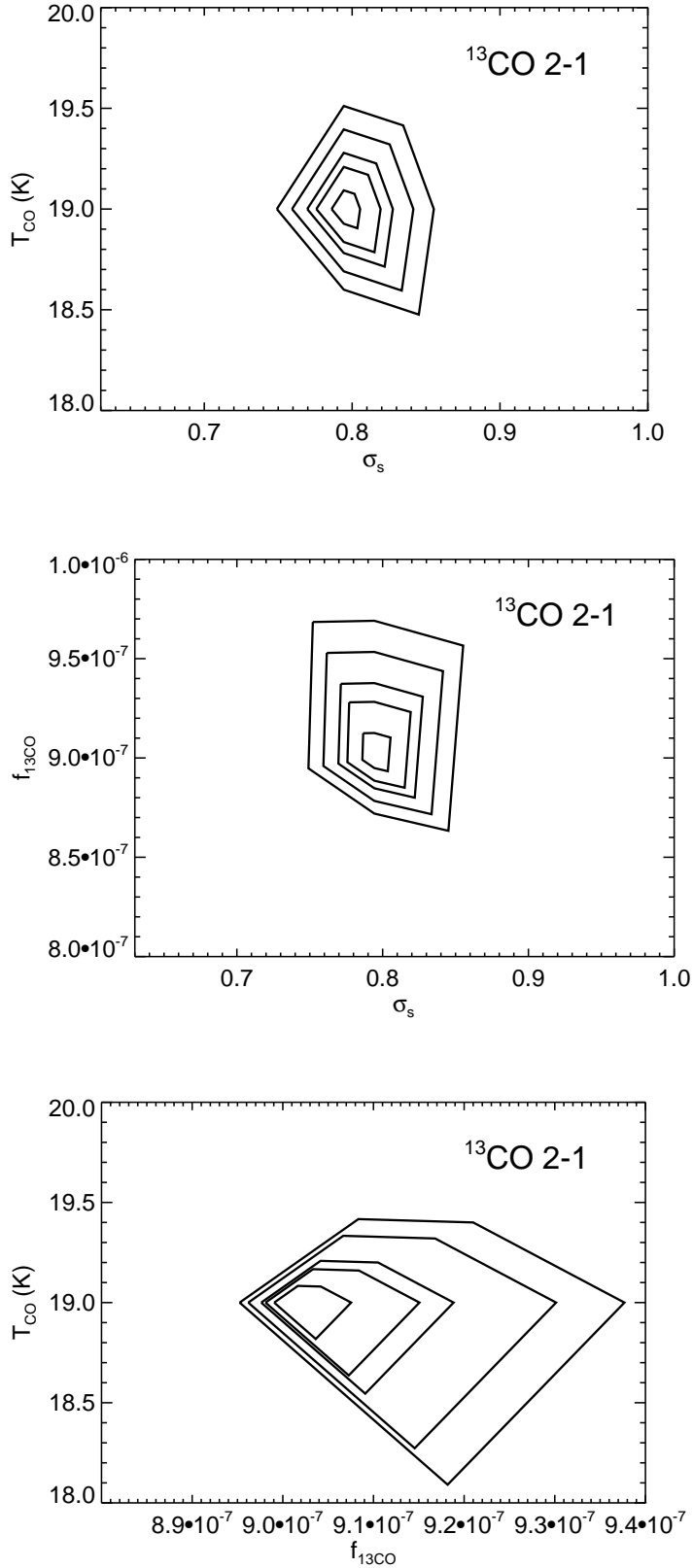


Fig. 10.— Iso- $\chi^2$  surfaces of CO freeze-out temperature ( $T_{\text{CO}}$ ), CO fractional abundance ( $f_{\text{CO}}$ ) and  $\sigma_s$  for  $^{13}\text{CO}$ . Contours correspond to the 1–5  $\sigma$  errors.

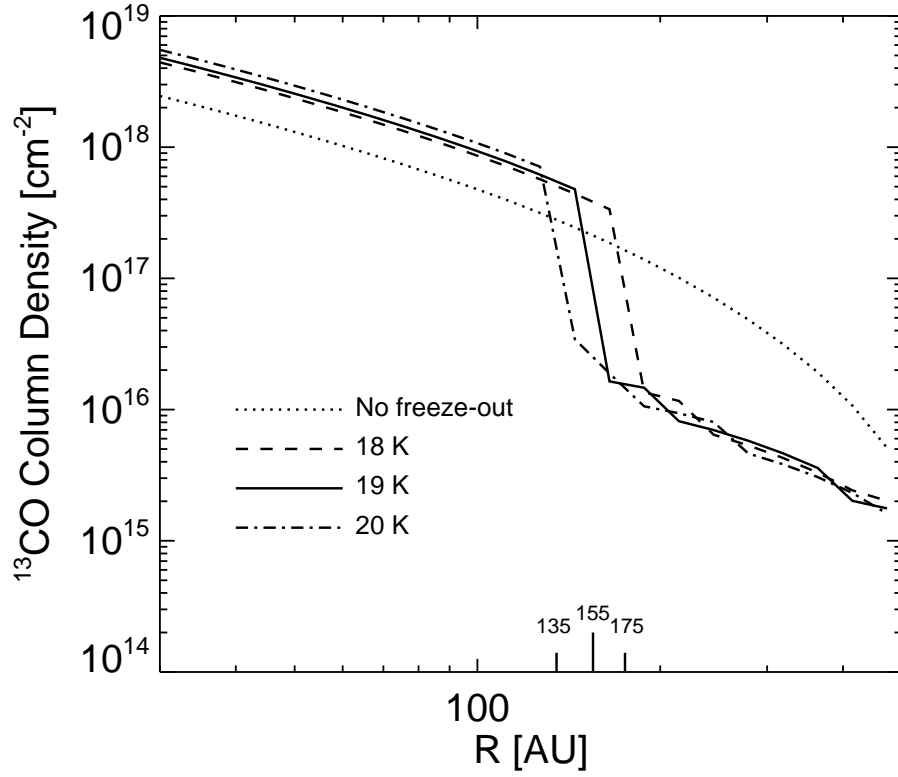


Fig. 11.— Models of  $^{13}\text{CO}$  radial column densities for no freeze-out (dotted), freeze-out at 18 K (dashed) 19 K (solid) and 20 K (dot-dashed). Each model has been scaled to fit the  $^{13}\text{CO}$  2–1 emission. Note that the CO snow line is at a radius of 155 AU for  $T_{\text{CO}} = 19$  K and it increases from 135 to 175 AU when  $T_{\text{CO}}$  decreases from 20 to 18 K.

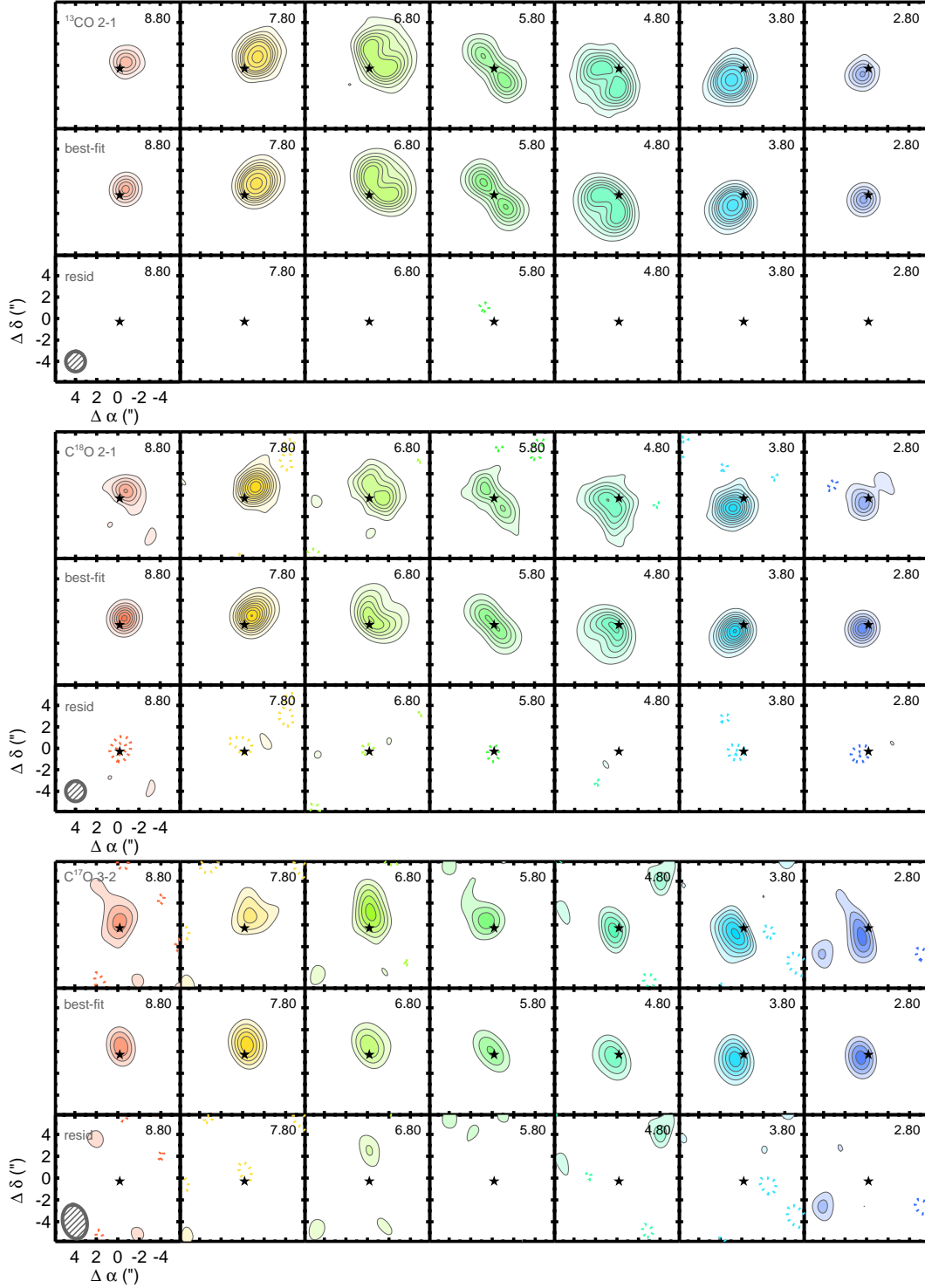


Fig. 12.— For each panel, the top rows are the velocity channel maps of the  $^{13}\text{CO}$ ,  $\text{C}^{18}\text{O}$  2–1 and  $\text{C}^{17}\text{O}$  3–2 emissions toward HD 163296, respectively (velocities binned in  $1 \text{ km s}^{-1}$ ). Contours are  $0.04 \text{ Jy Beam}^{-1} (1\sigma) \times [3, 6, 9, 12, 15, 18, 24, 30, 36, 42, 48, 54]$  for  $^{13}\text{CO}$  2–1;  $0.03 \text{ Jy Beam}^{-1} (1\sigma) \times [2, 4, 6, 8, 10, 12, 14, 16, 18, 20]$  for  $\text{C}^{18}\text{O}$  2–1;  $0.15 \text{ Jy Beam}^{-1} (1\sigma) \times [2, 3, 4, 5, 6, 7]$  for  $\text{C}^{17}\text{O}$  3–2. The middle rows are the best-fit models and the bottom rows are the difference between the best-fit models and data on the same contour scale.

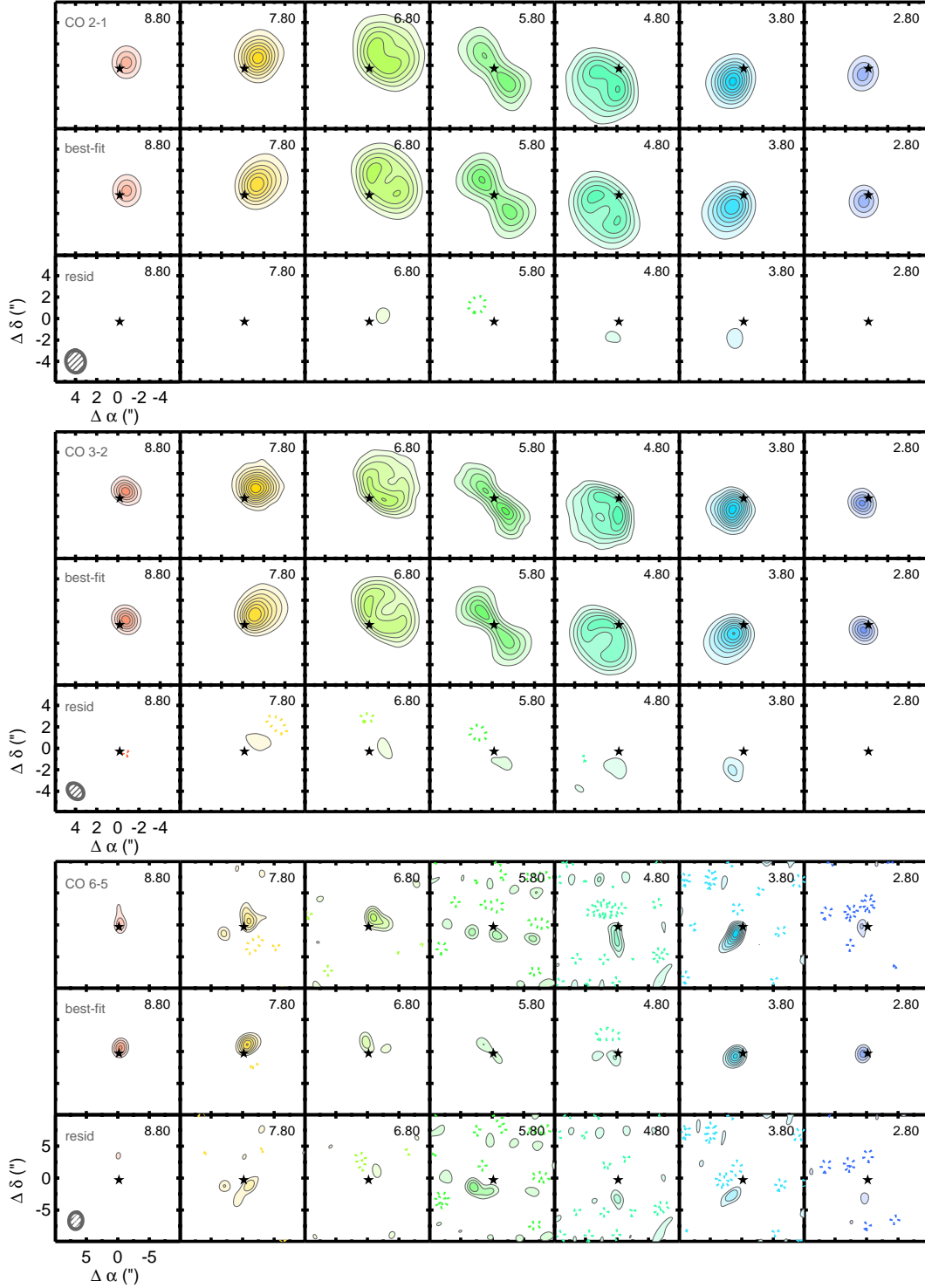


Fig. 13.— For each panel, the top rows are the velocity channel maps of the CO 2–1, 3–2 and 6–5 emissions toward HD 163296, respectively (velocities binned in  $1 \text{ km s}^{-1}$ ). Contours are  $0.15 \text{ Jy Beam}^{-1} (1\sigma) \times [3, 6, 9, 12, 15, 18, 21, 24]$  for CO 2–1;  $0.2 \text{ Jy Beam}^{-1} (1\sigma) \times [3, 6, 9, 12, 15, 18, 21, 24, 27]$  for CO 3–2;  $3.0 \text{ Jy Beam}^{-1} (1\sigma) \times [2, 3, 4, 5, 6, 7, 8]$  for CO 6–5. The middle rows are the best-fit models and the bottom rows are the difference between the best-fit models and data on the same contour scale.